

VYSOKÉ UČENÍ TECHNICKÉ V BRNĚ

BRNO UNIVERSITY OF TECHNOLOGY

FAKULTA STROJNÍHO INŽENÝRSTVÍ
FACULTY OF MECHANICAL ENGINEERING

ÚSTAV MATEMATIKY
INSTITUTE OF MATHEMATICS

NEW APPROACHES IN AIRBORNE THERMAL IMAGE
PROCESSING FOR LANDSCAPE ASSESSMENT
NOVÉ PŘÍSTUPY ZPRACOVÁNÍ LETECKÝCH OBRAZOVÝCH TERMÁLNÍCH DAT
K HODNOCENÍ KRAJINY

DIZERTAČNÍ PRÁCE
DOCTORAL THESIS

AUTOR PRÁCE
AUTHOR

Ing. MAREK PIVOVARNÍK

VEDOUCÍ PRÁCE
SUPERVISOR

doc. Mgr. Ing. FRANTIŠEK ZEMEK, Ph.D.

Abstrakt

TO DO...

Summary

TO DO...

Klíčová slova

dialkový prieskum Zeme, letecké termálne hyperspektrálne dátá, separácia teploty a emissivity

Keywords

remote sensing, airborne thermal hyperspectral data, temperature-emissivity separation

I declare that I have written the doctoral thesis *New Approaches in Airborne Thermal Image Processing for Landscape Assessment* on my own according to advice of my supervisor doc. Mgr. Ing. František Zemek, Ph.D., and using the sources listed in references.

May 15, 2012

Ing. Marek Pivovarník

Rád bych poděkoval doc. RNDr. Jaroslavu Michálkovi, CSc., za jeho vedení mé dizertační práce, veškerou ochotu a trpělivost, kterou mi věnoval, a v neposlední řadě za množství cenných rad nejen v odborných oblastech či k samotné dizertační práci. Mé poděkování patří také mým nejbližším za jejich podporu během celého studia.

Ing. Marek Pivovarník

Contents

Introduction	11
1 Theoretical Background on Thermal Radiation	13
2 Airborne Thermal Hyperspectral Data Properties	16
2.1 Instrument Technical Specifications	16
2.2 Image data pre-processing	17
3 Temperature and Emissivity Separation	24
3.1 Available approaches	24
3.2 Temperature and emissivity separation algorithm (TES)	26
3.3 TES Algorithm Improvement	27
4 OSTES Validation	31
4.1 Synthetic Data	31
4.2 Real Data	34
5 Ground Measurements	41
5.1 Introduction	41
5.2 Methods	43
5.3 Data Properties	44
5.4 Spectral Smoothing Algorithm	45
6 Conclusion	46
A Dependencies Between City Structure and Thermal Behaviour in Brno	48
B Spectral Emissivity Library of Spoil Substrates	52
B.1 Header	52
B.2 Spectral Emissivity	53
Bibliography	56

Introduction

Remote sensing, as the term used nowadays, refers to acquisition of information from airborne and satellite platforms. Acquired information is electromagnetic (EM) radiation emitted or reflected from Earth. It is a powerful tool for observing land surface, atmosphere and oceans which results in many applications in different fields such as meteorology, ecology, global change studies, agriculture, sociology, urban studies and many others [?J13?].

Remote sensing activities can be divided into groups according to the different regions of EM spectrum. The boundaries between EM regions are not sharply defined. According to Zemek et al. [72] the EM regions can be divided into visible ($0.4 - 0.72 \mu\text{m}$), near infrared ($0.72 - 1.3 \mu\text{m}$), short-wave infrared ($1.3 - 3 \mu\text{m}$), mid-wave infrared ($3 - 8 \mu\text{m}$), long-wave infrared ($8 - 14 \mu\text{m}$) and microwave ($1 \text{ mm} - 1 \text{ m}$). First three mentioned EM regions are mostly used for acquisition of reflected EM radiation. The EM radiation in long-wave infrared region, also widely called *thermal* infrared region, contains radiation, which is mainly emitted. Mid-wave infrared consists of mixture of reflected and emitted EM radiation. Microwave radiation is used by radar systems for active and passive remote sensing. Data acquisition is also limited by atmosphere transmittance, which can be very weak between individual regions.

According to the number of spectral bands and its widths, sensors are divided into broadband, multispectral and hyperspectral. Broadband sensors are continuously sensitive within the one region of EM spectrum, multispectral sensors consists of few, rather wide, spectral bands and hyperspectral sensors acquire data in many very narrow spectral bands.

The previous splittings set the scope for the contents of this treatise. The treatise focuses on theory and methodology for temperature and emissivity separation from data acquired by airborne thermal hyperspectral sensor. In other words, the data are acquired by airborne sensor recording emitted EM radiation in region of $8 - 14 \mu\text{m}$ in several narrow bands. Airborne thermal hyperspectral data offers valuable information, which is useful in fields focused on evapotranspiration [45], vegetation [47], soil moisture [53], mineral mapping [43], urban studies [58], gas plumes identification [?PM05?] and others.

The first airborne thermal multispectral sensor was developed in 1980 by NASA JPL. This sensor consists of five multispectral bands in thermal region. Currently operational airborne sensors are Airborne Hyperspectral Scanner (AHS 80) and Spatially Enhanced Broad Array Spectrograph System (SEBASS). To our best knowledge, there are currently three commercially available airborne thermal hyperspectral sensors, namely TASI (Itres Ltd., Calgary, Canada), AISA Owl (Specim Ltd., Oulu, Finland) and Hyper-Cam LW (Telops Inc., Quebec, Canada).

The treatise starts with theoretical background of thermal radiation. In the first section are mentioned fundamental laws and principles necessary for correct understanding of properties of data acquired by airborne thermal hyperspectral sensor. The interpretation of such a data is introduced in the second section together with description of main difficulty in temperature and emissivity separation. Third section offers overview of currently used algorithms for temperature and emissivity separation as well as methodologies for atmospheric corrections. In the fourth section are briefly mentioned preliminary results on

improvement of one of the temperature and emissivity separation algorithms mentioned in third section. The treatise is enclosed with definition of main aims of the doctoral thesis.

1

Theoretical Background on Thermal Radiation

This chapter describes fundamental principles and concepts of EM radiation called *thermal radiation*. Every object with temperature above 0 K emits thermal radiation. The amount of thermal radiation as a function of wavelength depends on object's temperature and its surface as is described in following text.

Black body

The concept of black body is very well described in the work of Howell [28], where black body is defined as perfect absorber for all incident radiation. Apart of perfect absorber, the black body is perfect emitter as well. Thus black body absorbs and reemits all energy incident upon it. Black body does not exist in nature but its concept is used for determination of real object's surface property called emissivity, which will be defined in following text.

Planck's law

Concerning black body at thermal equilibrium, the amount and spectral distribution of emitted energy is described by Planck's law [46]:

$$B(T, \lambda) = \frac{2hc^2}{\lambda^5} \frac{1}{e^{\frac{hc}{\lambda kT}} - 1},$$

where $B(T, \lambda)$ is spectral radiance ($\text{W m}^{-2} \mu\text{m}^{-1} \text{sr}^{-1}$) of black body at temperature T (K) and wavelength λ (μm); k is Boltzmann constant ($1.3806488 \cdot 10^{-23} \text{ J K}^{-1}$), h is Planck constant ($6.62606957 \cdot 10^{-34} \text{ Js}$) and c is speed of light ($299792458 \text{ m s}^{-1}$). Example of the black body radiation at three different temperatures, as described by Planck's law, is depicted in figure 1.1a.

Emissivity

The emissivity is defined as ratio of radiance of real surface to that of black body at the same temperature:

$$\varepsilon(T, \lambda) = \frac{L(T, \lambda)}{B(T, \lambda)},$$

where $\varepsilon(T, \lambda)$ is spectral emissivity and $L(T, \lambda)$ is real surface spectral radiance. The emissivity can be understood as real surface emission effectiveness in comparison with radiation emitted by a black body of the same temperature in the same wavelength. Let us note that emissivity depends on the viewing angle apart temperature and wavelength, as is defined in Hollow [28]. In remote sensing an observed objects are of the temperature within 270 – 330 K and the observation angle is close to nadir (usually maximum off-nadir angle is less than 30°), which causes negligible changes in spectral emissivity of most of the natural surfaces. Thus, it can be further assumed that emissivity depends just on wavelength.

Quartz was chosen to demonstrate the principles of radiation of real object's surfaces. Its spectral emissivity was taken from ASTER spectral library [2] and it is shown in the figure 1.1b. Quartz heated to the temperature T has spectral radiance $L(T, \lambda) = \varepsilon(\lambda)B(T, \lambda)$ as is illustrated in figure 1.1c.

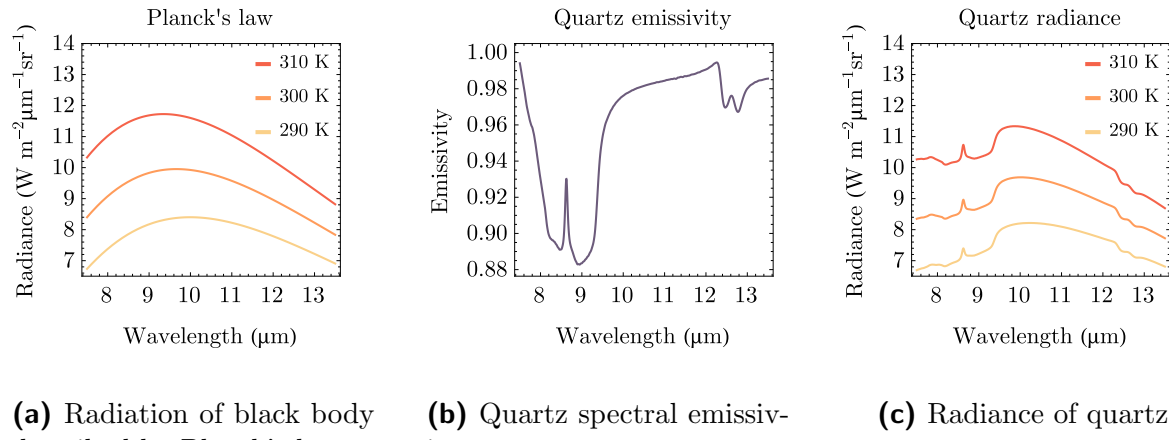


Figure 1.1: Principles of radiation of real surfaces.

Wien's displacement law

The peak of black body radiation at wavelength λ_{max} is described by Wien's displacement law [28]:

$$\lambda_{max} = \frac{b}{T},$$

where b is Wien's displacement constant (2.8977721 m K). As was mentioned before, the temperature of the most of the natural and artificial surfaces observed by airborne remote sensing ranges in 270 – 330 K. According to the Wien's displacement law, the peak of emitted radiation varies roughly from 8.8 μm to 10.7 μm . This range is in coincidence with the atmospheric window situated between 8 μm to 13 μm . The atmospheric transmittance in this atmospheric window is very high and thus it is relevant for acquisition of remotely sensed thermal data.

Kirchhoff's law of thermal radiation

Emitting and absorbing properties of an object at local thermodynamic equilibrium surrounded by isothermal environment are tied up by Kirchhoff's law of thermal radiation

[38]. It states that object's surface absorptivity $\alpha(\lambda)$ at a given wavelength equals to object surface emissivity $\varepsilon(\lambda)$ at the same wavelength:

$$\alpha(\lambda) = \varepsilon(\lambda).$$

Energy conservation implies that energy incident to the object surface can be reflected, transmitted or absorbed. Considering the fractions of incident energy the following equation holds:

$$1 = \rho(\lambda) + \tau(\lambda) + \alpha(\lambda),$$

where $\rho(\lambda)$ is objects surface spectral reflectivity, $\tau(\lambda)$ is object surface spectral transmissivity and $\alpha(\lambda)$ is object surface spectral absorptivity. Applying Kirchhoff's law to opaque material ($\tau(\lambda) = 0$) results in following equation:

$$1 = \rho(\lambda) + \varepsilon(\lambda) \Rightarrow \rho(\lambda) = 1 - \varepsilon(\lambda).$$

All mentioned principles in this section will be further used in explanation of properties of airborne thermal hyperspectral data and its processing.

2

Airborne Thermal Hyperspectral Data Properties

This chapter provides insights into technical parameters of Thermal Airborne Spectrographic Imager (TASI) and processing chain of image data acquired by this sensor. Knowledge of the instrument parameters and processing chain gives important overview of the image data properties and their components. The result of the processing chain described in this chapter is georeferenced image data containing land-leaving radiance. Such an image data form input for further processing. Let us note that this chapter omits naming physical quantities dependent on wavelength as “spectral” for the sake of clarity. However, all quantities remain wavelength dependent.

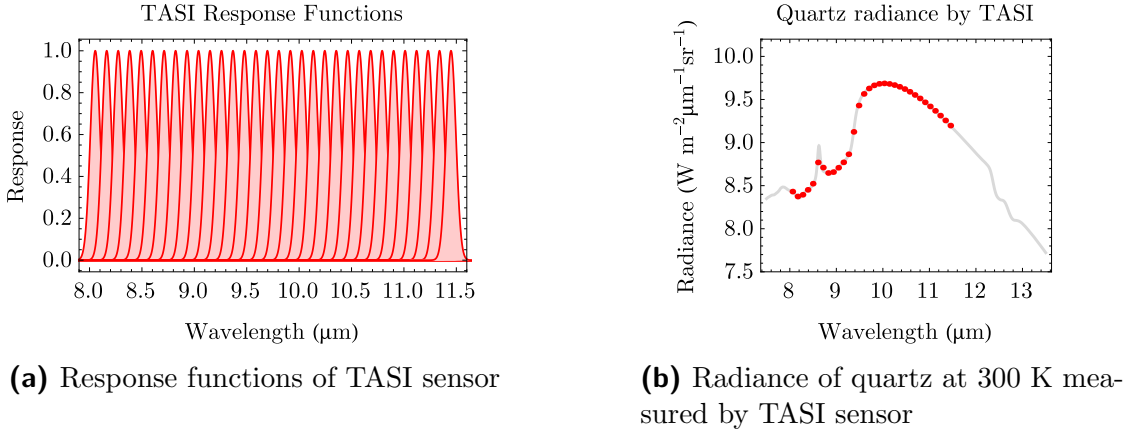
2.1. Instrument Technical Specifications

The TASI sensor is developed by Itres Ltd. (Calgary, Canada) and is one of the very few commercially available pushbroom hyperspectral TIR sensors equipped with mercury cadmium telluride array. Each of its 600 across-track imaging pixels contains 32 bands all of which are in the TIR region. Bands are situated in the 8 to 11.5 μm region and have a FWHM $\approx 0.11 \mu\text{m}$ with $\text{NE}\Delta\text{T} \approx 0.1 \text{ K}$. The response functions of the TASI sensor are described by the Gaussian functions as depicted in Figure 4.1.

The shape of response functions implies that any quantity observed by TASI sensor is of finite spectral-bandwidth. Quantities needs to be transformed to band-effective quantities in order to relate them with certain wavelength. The band-effective quantities are obtained by using weighted average:

$$X_i = \frac{\int_{\lambda_1}^{\lambda_2} r_i(\lambda) X(\lambda) d\lambda}{\int_{\lambda_1}^{\lambda_2} r_i(\lambda) d\lambda}, \quad (2.1)$$

where $r_i(\lambda)$ is response function of band i , λ_1 and λ_2 are lower and upper boundaries of band i and X can be substituted by any quantity. In Figure 2.6b is illustrated radiance of quartz (solid line) and band-effective values of radiance measured by the TASI sensor (red dots). Sensor of this type is available at Global Change Research Institute CAS (Brno, Czech Republic) and it is a part of Flying Laboratory of Imaging Systems (FLIS) [24].

**Figure 2.1:** TASI response functions.

2.2. Image data pre-processing

The main objective of image data pre-processing is transformation of acquired raw image data into the georeferenced radiance at-surface level. It is accomplished by three major steps: radiometric calibration, atmospheric corrections and geometric pre-processing. Radiometric calibration converts digital numbers (DN) into values of radiance at-sensor level. Atmospheric corrections compensates the influence of intervening atmosphere and produces land-leaving radiance. Finally, the geometric pre-processing compensates for image data distortions caused by aircraft movement and register image data into coordinate system.

Supportive field measurements of thermal radiance, temperature, emissivity and atmospheric parameters offers valuable data for calibration and validation purposes. Especially in cases of airborne image data for scientific purposes the high quality is strongly demanding. Thus it is necessary to perform supportive measurements in order to achieve precise results and determine the data quality.

It is important to emphasize, that currently does not exist any definitive standard pre-processing chain. It is caused mainly by huge number of sensors with various technical parameters and their different applications. Sensors usually have tailored pre-processing chains, which is the case of TASI sensor as well. Certain parts of processing chain are maintained by commercial tools. However, there are still parts of processing chain, which needs to be done by in-house tools. In Figure 2.2 is illustrated processing chain used in Global Change Research Institute CAS (Brno, Czech Republic) to pre-process image data acquired by TASI sensor. Individual parts of the diagram will be discussed in the following text.

2.2.1. Radiometric Calibration

Thermal radiation incident upon the sensor array originates from many additive components (e.g. observed scene, instrument enclosure, intervening atmosphere and others). Incident thermal radiation produces electrical signal, which is proportional to radiant intensity. Electrical signal is then amplified and converted into voltage and subsequently into DN values. Radiometric calibration consists of separating signal from viewed scene

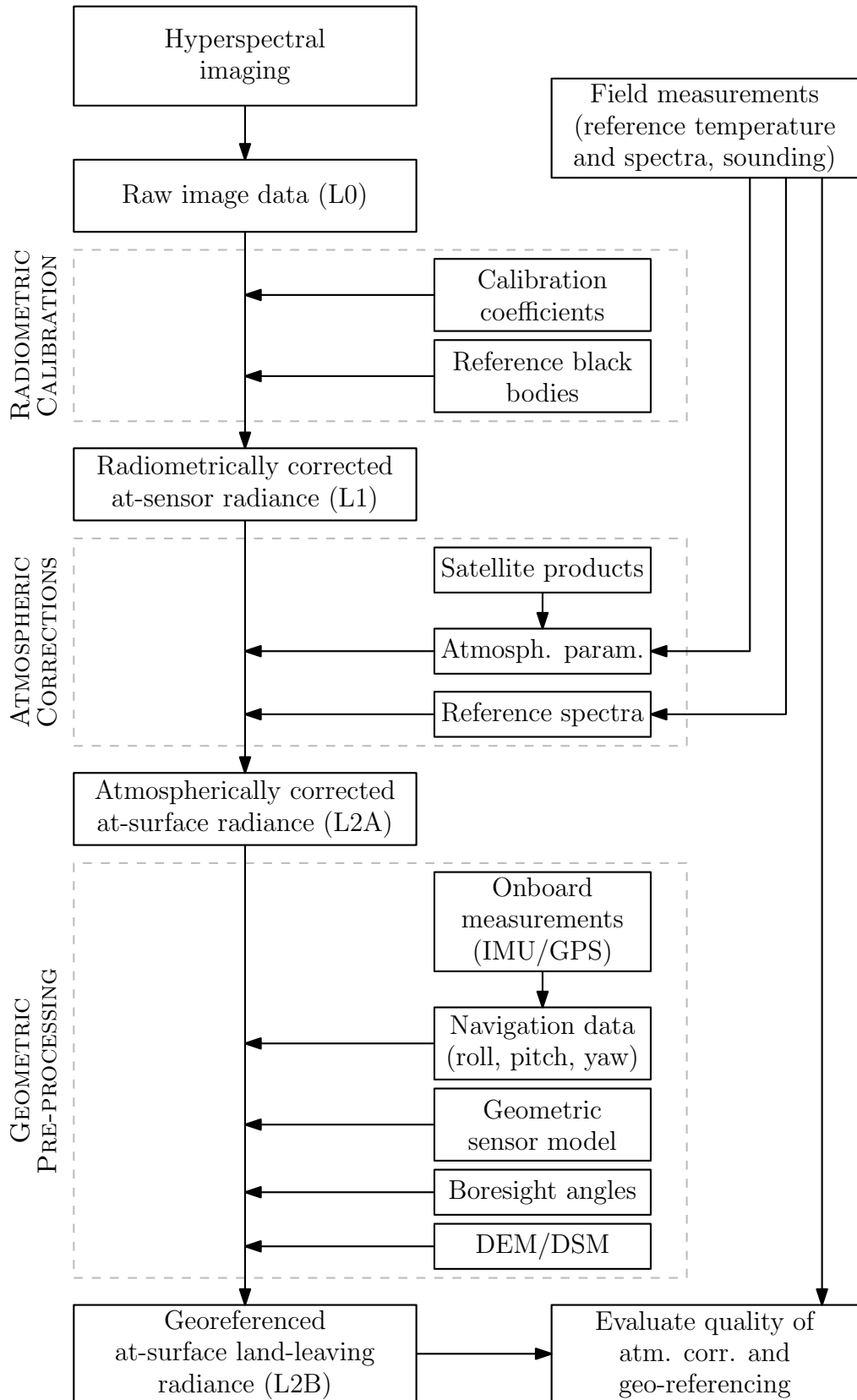


Figure 2.2: Processing chain applied to image data acquired by TASI sensor.

and converting it into physical units of radiance. Atmosphere influence is not accounted in this process and thus after radiometric calibration one gets radiance at-sensor level.

The relationship between DN and at-sensor radiance L_m is following:

$$DN = a + bL_m,$$

where a and b are calibration coefficients. The calibration coefficient a , also known as offset, represents radiation originating from instrument enclosure, sensor dark current and electronic offset. The calibration coefficient b , also called gain, determines sensor radiant sensitivity. Calibration coefficients are determined by imaging a set of reference black bodies of known temperature and emissivity. In this context, the term black body is meant to be a surface with emissivity very close to unity. These coefficients are usually determined applying one of two methods: 1) imaging two black bodies at different temperature directly before imaging, or 2) combining black body image data from laboratory and black body image data acquired before imaging.

In the first case are usually used two black bodies of different temperatures. Temperatures of these black bodies enclose temperatures expected to occur in the scene. Let us consider the radiance of cold black body $L(T_C)$ and the radiance of hot blackbody $L(T_H)$. The calibration coefficients can be obtained from:

$$\begin{aligned} a &= \frac{DN_H L(T_C) - DN_C L(T_H)}{L(T_C) - L(T_H)} \\ b &= \frac{DN_C - DN_H}{L(T_C) - L(T_H)}, \end{aligned}$$

where DN_C and DN_H are digital numbers measured by sensor viewing cold black body and hot black body respectively. This procedure is commonly used in case of other instruments for measuring thermal radiation, such as μ FTIR [26].

The determination of calibration coefficients in the second case assumes that gain calibration coefficient b does not change under different conditions. Thus, it is sufficient to perform series of black body measurements at different temperatures in order to determine gain calibration coefficient b . These measurements can be performed in the laboratory once per season. However, offset calibration coefficient a does not remain stable and changes under different conditions. Hence, it is necessary to image a black body at known temperature directly before acquisition to account for variability of this coefficient.

Again, it is important to emphasize that all quantities and both calibration coefficients are wavelength dependent. Spectral calibrations are part of the radiometric calibrations. In the laboratory are determined band centers of every pixel using laser at different wavelengths. Determined positions does not change over time significantly. However, the spectral shift occurs under different conditions and thus it needs to be determined for every scene. Spectral shift estimation is usually based on the spectral features of the atmosphere or certain materials.

In case of TASI sensor are used commercial softwares delivered by Itres company (Calgary, Canada). SparCal software [31] is used to determine all parameters necessary for radiometric calibrations from laboratory measurements. RCX software [32] is used for additional estimation of calibration parameters and for processing raw image data. Both softwares are tailored for the TASI sensor. The resulting image data are made of radiance at-sensor level L_m .

2.2.2. Atmospheric Corrections

Radiometric calibrations deliver image data containing radiation from the surface, attenuated by atmosphere, plus radiation from the atmosphere along the line of sight. Thus the measured radiance at-sensor level (L_m) consists mainly of radiance emitted from the land surface, downwelling atmospheric radiance reflected by the surface (L_{atm}^{\downarrow}) and the atmospheric upwelling radiance (L_{atm}^{\uparrow}). The sum of all these components is expressed by a radiative transfer equation (RTE) as follows:

$$L_m = \tau\varepsilon B(T_s) + \tau(1 - \varepsilon)L_{atm}^{\downarrow} + L_{atm}^{\uparrow}, \quad (2.2)$$

where $B(T_s)$ is radiance of the surface at temperature T_s according to the Planck's law, ε is the surface's emissivity and τ is atmospheric transmittance. It is important to emphasize that all elements in the equation are wavelength dependent but notation for this is omitted for the sake of clarity. Since sensors are of finite bandwidth, quantities in (2.2) are replaced by band-effective equivalents according to the (2.1). Moreover, RTE can be used under the assumption of cloud-free atmosphere under local thermodynamic equilibrium. The meaning of the RTE is illustrated in the Figure 2.3, where ρ is reflectivity. Kirchhoff's law of thermal radiation implies that reflectivity ρ can be rewritten as $(1 - \varepsilon)$ for opaque materials.

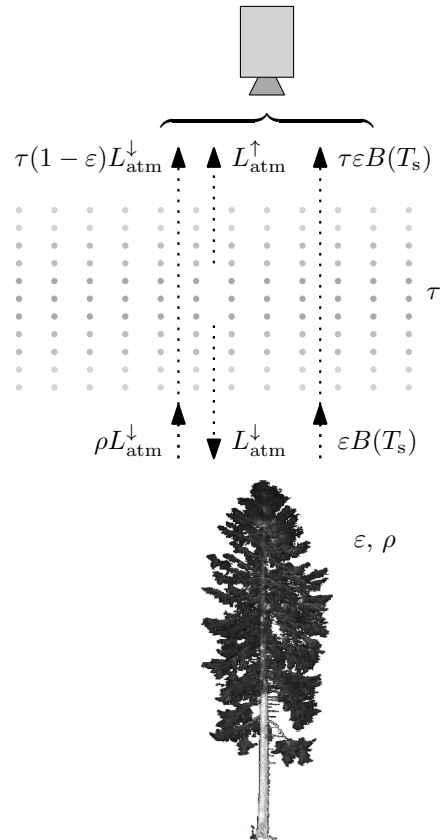


Figure 2.3: The radiance incident to the sensor in the thermal region originates mainly from three sources: 1) radiance $\tau\varepsilon B(T_s)$ emitted by object; 2) reflected downwelling atmospheric radiance $\tau(1 - \varepsilon)L_{atm}^{\downarrow}$; 3) upwelling atmospheric radiance L_{atm}^{\uparrow} emitted by atmosphere itself.

The goal of the atmospheric corrections is to determine atmospheric transmittance, downwelling and upwelling atmospheric radiance and compensate for them. The quantifi-

cation of these quantities are usually based on radiative transfer models of the atmosphere. For this purpose is usually used MODerate resolution atmospheric TRANsmision (MODTRAN) model [4]. MODTRAN simulates atmospheric parameters such as atmospheric transmittance, downwelling and upwelling atmospheric radiance based on input parameters such as vertical profiles of water vapour content and temperature, CO₂ concentration, the choice of model atmosphere (if measured profiles are not available) and many others. In general, input parameters can be obtained in two ways: 1) by in-situ measurements; 2) by satellite-based products.

The most common in-situ measurement is radio sounding. Radiosonde is launched during the overflight and it is used to measure vertical temperature and water vapour profile of the atmosphere. Other in-situ instruments can be used as well, for example sun-photometer for obtaining water vapor content or different radiometers for measuring sky or surface radiance. Other source of water vapour and temperature profile is satellite-based products acquired close to the time of aircraft overflight. The most common is MOD07_L2 product [5] generated by Moderate Resolution Imaging Spectroradiometer (MODIS) instrument. Illustration of the transmittance, downwelling and upwelling atmospheric radiance generated by MODTRAN using MOD07_L2 products as input are depicted in Figure 2.4.

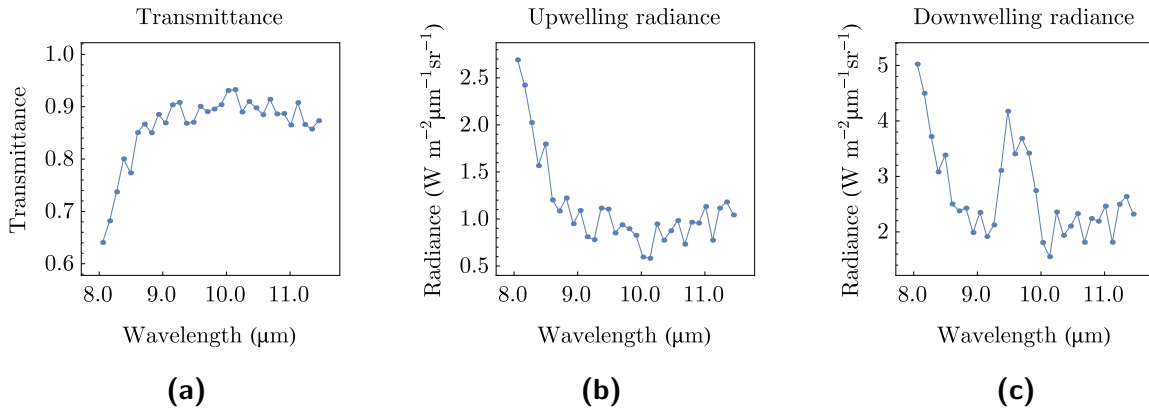


Figure 2.4: Example of atmospheric parameters used for atmospheric correction of TASI image data acquired at altitude of 2000 m during summer season.

In case of thermal hyperspectral images, various algorithms for estimating atmospheric effects based just on the image data itself were developed. Usually it is applied to one of the following: In-Scene Atmospheric Corrections (ISAC) introduced by Young et al. [71] and Autonomous Atmospheric Compensation (AAC) introduced by Gu et al. [22]. The advantage of using one of these algorithms is that no supporting data are necessary. The drawback of these methods remains in estimation of just atmospheric transmittance and upwelling atmospheric radiance.

Once all the atmospheric parameters are determined, it remains to compensate for them. Compensating for atmospheric transmittance and upwelling atmospheric radiance lead to land-leaving radiance:

$$L_{\text{LL}} = \varepsilon B(T_s) + (1 - \varepsilon)L_{\text{atm}}^{\downarrow}. \quad (2.3)$$

The downwelling atmospheric radiance is not possible to separate without knowledge of emissivity. Hence, image data after atmospheric corrections are made of land-leaving radi-

ance L_{LL} . Compensation for downwelling atmospheric radiance is part of the temperature and emissivity separation described in Chapter 3.

Atmospheric corrections for TASI sensor, as part of processing chain, are not performed by commercial products. However, there exists commercial tools that allows complex solution for atmospheric corrections. An example of such a tool is ATCOR [48] which is based on look-up tables generated by MODTRAN and takes into account terrain topography and sensor parameters. It offers basic temperature and emissivity separation algorithms as well. Apart of mentioned solution, atmospheric corrections rely on extracting data from in-situ measurements or satellite products, running radiative transfer models and applying derived atmospheric parameter on image data. Alternatively, algorithms for atmospheric parameters estimation from image data can be implemented. In both cases, atmospheric corrections involve creating in-house tools.

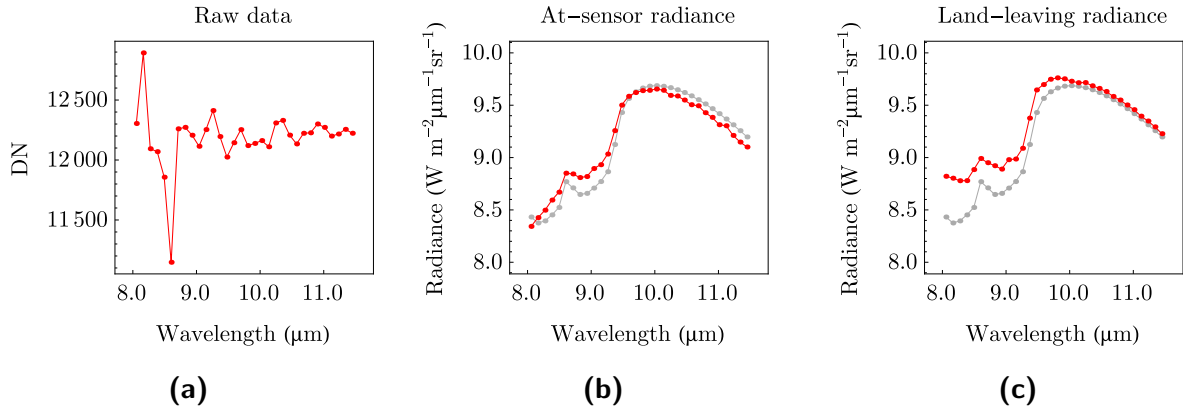


Figure 2.5: Example of data at various processing stages. Data simulates quartz at 300 K as would be acquired by TASI sensor at altitude of 2000 m under summer mid-latitude atmosphere. Case (a) shows raw data, case (b) shows data after radiometric calibration (in red) and case (c) shows data after corrections of atmospheric transmissivity and upwelling atmospheric radiance (in red). In cases (b) and (c) are shown pure quartz radiance in gray.

2.2.3. Geometric Pre-processing

Acquired image data are distorted during its acquisition and geometric pre-processing is accounting for all factors causing these distortions. During geometric pre-processing are taken into account aircraft motion, terrain variations and geometric sensor model in order to register image data into reference frame.

Ancillary data about aircraft position and movement, terrain structure and geometric sensor model are necessary. Aircraft needs to be equipped with IMU/GNSS systems for recording aircraft position (longitude, latitude and altitude) and orientation (roll, pitch and heading angles). Terrain structure is obtained form Digital Surface Model (DSM) or Digital Elevation Model (DEM). These data are derived from aerial laser scanning or from stereo images. Aerial laser scanning can be performed either simultaneously with image data acquisition or separately. Other sources of DEM/DSM are national services or satellite products (e.g. ASTER product AST14DEM). Geometric sensor model is usually delivered by sensor manufacturer.

The process applied on image data during geometric pre-processing is called georeferencing. It consists of two successive steps: direct image data geocoding and resampling. Direct image data geocoding consists of geometric corrections and orthogonalization of the image data. These are further resampled into regular grid of the reference frame with the desired coordinate system (e.g. Universal Transverse Mercator coordinate system). Image data are resampled into desired spatial resolution applying nearest neighbor, bilinear or cubic interpolation. For the scientific purposes is commonly used nearest neighbor interpolation since it preserves spectral information and does not combine spectra from surrounding pixels.

Geometric pre-processing of the image data acquired by TASI sensor are performed by GeoCor software [33] delivered by Itres company (Calgary, Canada). Importance of image data geometric pre-processing is illustrated in the Figure 2.6.

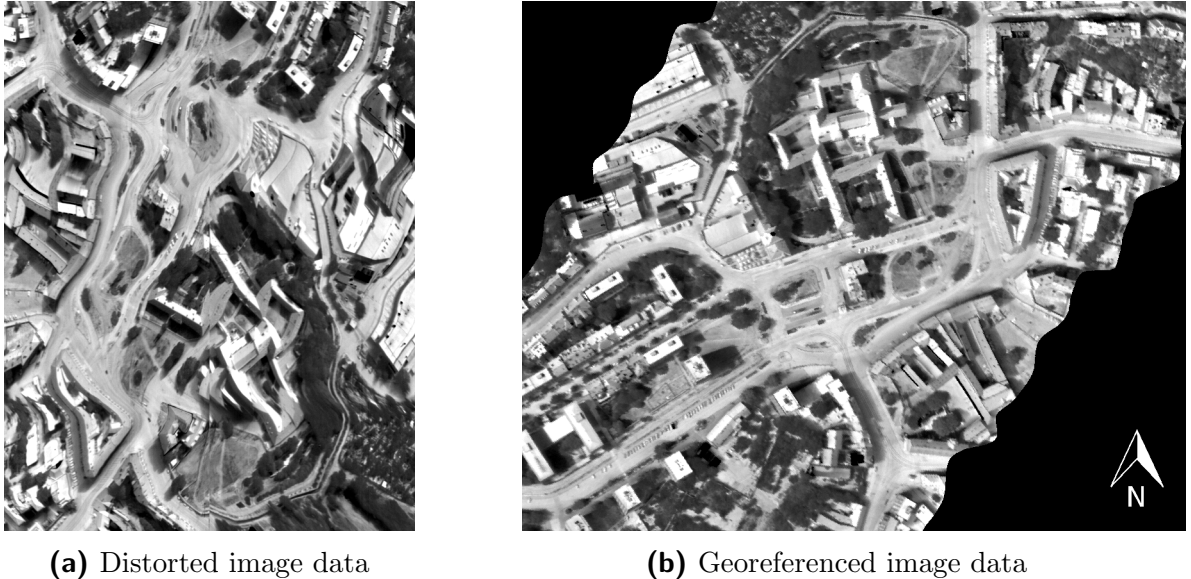


Figure 2.6: Illustration of land-leaving radiance image data before and after geometric pre-processing.

3

Temperature and Emissivity Separation

Pre-processed thermal image data provide valuable information about the properties of the observed surfaces, most importantly their temperature and emissivity. But in order to determine temperature and emissivity from observed radiance one must solve system of RTEs. Data from multispectral and hyperspectral TIR sensors offer the opportunity to derive both the temperature as well as an emissivity spectrum, which can be used to characterize the material composition of surfaces. However, observing radiance in N bands yields N RTEs but $N + 1$ unknowns (N emissivities plus temperature), which results in the underdetermined system of equations. The estimation of temperature and emissivity from such a system of equations is usually addressed as *temperature-emissivity separation*. This chapter describes several approaches for separating temperature and emissivity. It firstly introduces few commonly used ones and then focuses on the most popular approach called Temperature and emissivity separation algorithm (TES). Last part of this chapter focuses on enhancing the accuracy and precision of the products generated by the TES algorithm. The main improvement is accomplished by replacing one of the TES modules with a newly designed one that takes advantage of a relationship between brightness temperature and emissivity. The improved TES algorithm is called Optimized Smoothing for Temperature Emissivity Separation (OSTES).

3.1. Available approaches

Many approaches have been developed to overcome the problem of having an underdetermined system of RTEs [40]. Methods used to overcome the problem of underdetermined system of RTEs are usually based on adding empirical or semiempirical constraints.

Algorithms for temperature and emissivity estimation depend on sensor architecture and acquisition context. Some algorithms require knowledge of Normalized Difference Vegetation Index (NDVI) [59], surface type [52] or even emissivity [34]. Others are based on multitemporal [68] or multiangle [60] acquisition. There are only a small number of algorithms for simultaneous temperature and emissivity retrievals from a single scene without ancillary surface information, that are robust enough to be applicable to data acquired by multispectral or hyperspectral sensors. The most common are: grey body emissivity method [3], linear emissivity constraint temperature emissivity separation method [69], spectral smoothing [7] and the TES algorithm [21]. Principles of last four mentioned methods are described in the following text. The most attention is paid to the TES algorithm, as it is the most popular and it is widely applied to many sensors.

Gray body emissivity method

Barducci and Pippi [3] proposed algorithm, which is based on assumption of flat spectral emissivity beyond $10\text{ }\mu\text{m}$. To solve the system of RTEs it is enough to find at least two spectral bands with the same emissivity. This can be achieved in case of airborne thermal hyperspectral data. Drawback of this method is its sensitivity to instrument noise.

Linear emissivity constraint temperature emissivity separation method

As Wang et al. [69] describe, this method is based on idea of substituting spectral emissivity with piecewise linear function. The emissivity spectrum is divided into segments, in which spectral emissivities are assumed to be linearly dependent on wavelength. Thus, it is necessary for every segment to estimate gain and offset. It implies that the number of spectral bands has to be equal or greater than number of unknowns resulting from segmentation to piecewise linear functions.

Spectral smoothing

Spectral smoothing algorithm, also known as ARTEMISS (Automatic Retrieval of Temperature and Emissivity using Spectral Smoothness), was reported by Borel at [6] and [7]. Algorithm is based on the assumption that spectra of solids are much more smoother than spectra of gases. Thus by smoothing spectra one removes spectral features introduced by atmosphere and obtains spectral emissivity. Moreover, current implementation described in [7] includes modified ISAC algorithm called ARTISAC, which estimates atmospheric transmissivity for further choice correct atmospheric model. Atmospheric models contains so called TUD (atmospheric Transmissivity, Upwelling and Downwelling atmospheric radiance) and are stored in look-up tables (LUT). Then temperature is varied until the spectral emissivity is the smoothest possible, where the smoothness criterion is standard deviation of measured radiance minus simulated radiance. Spectral smoothness method can be described briefly by following steps:

1. estimation atmospheric transmissivity using ARTISAC algorithm
2. determination few closest atmosphere models from TUD-LUT according to the estimated atmospheric transmissivity
3. use these atmosphere models as input to spectral smoothness algorithm for a few pixels chosen from the image and the atmosphere model which results in smoothest emissivity in the most of the cases is chosen as the correct one
4. use chosen atmosphere model for the whole image and estimate temperature and emissivity by applying spectral smoothing procedure

3.2. Temperature and emissivity separation algorithm (TES)

TES algorithm was originally developed for the Advanced Spaceborne Thermal Emission and Reflection Radiometer (ASTER) sensor [21]. ASTER was launched in December 1999 onboard NASA's Terra platform. TES has since then found widespread use with other multispectral and hyperspectral sensors. Several studies have discussed the implementation of TES with Airborne Hyperspectral Scanner (AHS) data [56, 35]. Application of TES to data acquired by the TASI sensor is mentioned in a few studies as well [70, 45]. Apart from the mentioned sensors, the TES algorithm has been modified for the Digital Airborne Imaging Spectrometer (DAIS) sensor [55]. Concerning spaceborne sensors, the TES algorithm has also been suggested for Spinning Enhanced Visible and Infrared Imager (SEVIRI) [36], Moderate Resolution Imaging Spectroradiometer (MODIS) [29] and Multispectral Thermal Imager (MTI) [42] data processing. Moreover, the TES algorithm is being suggested for the future HyspIRI mission [30].

The TES algorithm is based on a semi-empirical relationship between spectral contrast (i.e. difference between the highest and lowest values in the emissivity spectrum) and the minimum emissivity. The algorithm consists of three modules, namely the Normalization Emissivity Module (NEM) [18], the Ratio module and the Maximum-Minimum Difference (MMD) module [41]. The inputs of the algorithm are land-leaving radiance L_{LL} and downwelling radiance L_{atm}^{\downarrow} . Let us remind the reader that land-leaving radiance is obtained from (2.2) by compensating for atmospheric transmissivity τ and atmospheric upwelling radiance L_{atm}^{\uparrow} :

$$L_{LL} = \varepsilon B(T_s) + (1 - \varepsilon)L_{atm}^{\downarrow}. \quad (3.1)$$

The NEM module performs an iterative process for estimating temperature and emissivity, and compensating for the downwelling radiance. The output of the NEM module is an initial estimation of temperature and emissivity. Then the ratio module normalizes the emissivities obtained by the NEM module by their arithmetic mean. Thus one obtains the so called β spectrum, which should be less sensitive to sensor noise. Finally, the maximum and minimum of the β spectrum are found and their difference (MMD) is used in following semi-empirical relationship:

$$\varepsilon_{min} = 0.994 - 0.687 \times MMD^{0.737}. \quad (3.2)$$

Derivation of (3.2) is explained in following paragraph. Ratioing the β spectrum back to an emissivity spectrum with knowledge of minimum emissivity results in a more precise estimation of the emissivity spectrum. The band with highest emissivity is then used for temperature estimation.

The relationship between spectral contrast and minimum emissivity, shown in (3.2), is a regression based on 86 laboratory spectra of rocks, soils, vegetation, snow and water chosen from the ASTER spectral library [2]. This relationship is depicted in the Figure 3.1. It is important to note that (3.2) is tailored for the ASTER sensor. To apply TES to a different sensor, the regression of ε_{min} on MMD must be refined by using sensor specific response functions.

After ASTER was launched, [23] and [49] suggested to replace the power regression shown in (3.2) with linear regression. The replacement is connected with modification of

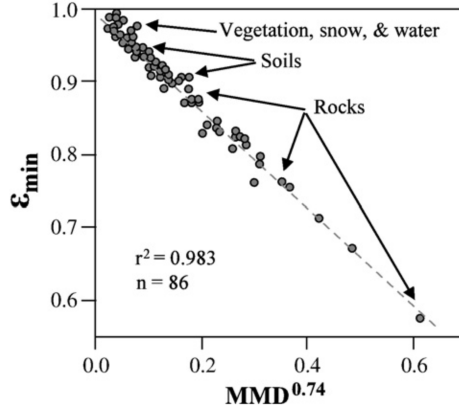


Figure 3.1: Semi-empirical relationship between emissivity contrast and minimum spectral emissivity as shown in study reported by Sabol et al. [49].

the threshold for separating materials with low spectral contrast. The main advantage is elimination of artefacts in retrievals. However, the drawback is loss of accuracy in cases of materials with low spectral contrast [49]. The TES algorithm used for generation ASTER standard products [1], as well as its modifications for other sensors [56, 35, 70, 55, 36, 29, 42, 30], is based on the power law regression. Thus, in this work the TES algorithm is considered to be that using the power regression.

3.3. TES Algorithm Improvement

The algorithm described below brings a new approach for the TES algorithm by replacing the NEM module with a completely new module. The new module is based on the similarity between brightness temperature spectral features and emissivity spectral features. Brightness temperature is obtained from land-leaving radiance under the assumption of emissivity $\varepsilon = 1$ for every wavelength. Although land-leaving radiance includes some portion of reflected downwelling radiance, it still retains the spectral features arising from the emissivity of the surface materials, which is 0.6 or higher for natural materials [21]. Since the magnitude of downwelling radiance is usually much lower than the surface radiance the features contained in the brightness temperature spectra may be distorted but will not be completely hidden. The new module approximates this relation between brightness temperature T_b and emissivity.

In order to demonstrate the relationship, three emissivity samples with different spectral contrasts were chosen from the ASTER spectral library [2], namely green grass, fine sandy loam and altered volcanic tuff. Emissivities are depicted in Figure 3.2 (solid lines) together with corresponding band-effective values for TASI sensor (empty symbols). These emissivities were applied to Plank's law at temperature 300 K and combined with downwelling radiance from standard mid-latitude summer atmosphere generated by MODerate resolution atmospheric TRANsmission (MODTRAN) [4]. The resulting radiances, were transformed to band-effective quantities with respect to TASI response functions. Brightness temperatures for every band of each sensor were obtained by applying inverse Planck's law on sample land-leaving radiances under the assumption of $\varepsilon = 1$. Figure 3.2 also includes brightness temperatures (full symbols) in order to demonstrate spectral similarity with emissivity. Figure 3.3 plots emissivity against brightness temperature for

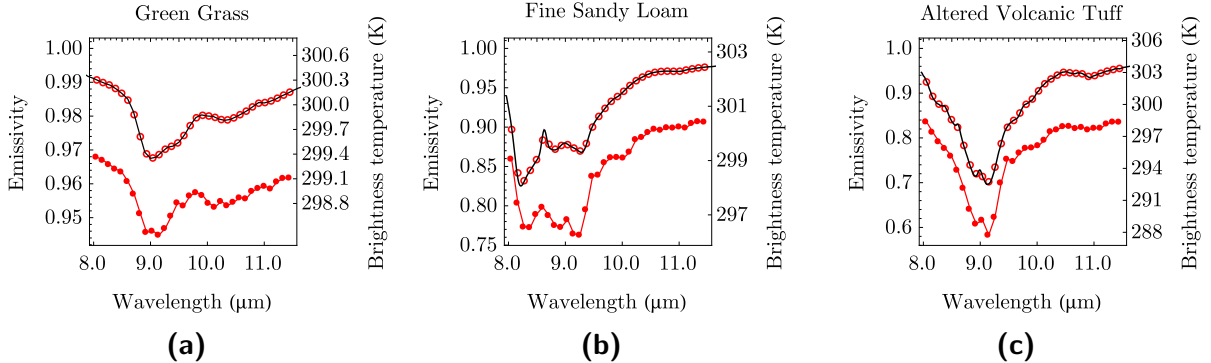


Figure 3.2: Emissivity spectra (black solid line) of three samples chosen from ASTER spectral library [2]. Symbols represent band-effective values of emissivity (empty symbols) and brightness temperature (full symbols) for TASI sensor.

chosen samples (empty symbols). These quantities clearly exhibit relationship with linear trend regardless of spectral contrast. Figure 3.3 also displays lines that approximate this relationship, derived in the manner described later in the next. The algorithm description below uses band-effective values of quantities linked to i -th band by subscript index i .

Spectral features of brightness temperature will be further used for emissivity estimation. The dependence of emissivity ε_i on brightness temperature T_{b_i} will be approximated by following equation:

$$\varepsilon_i = pT_{b_i} + q, \quad (3.3)$$

where p and q are empirical coefficients. These coefficients are determined by solving the system of two equations using two points, namely maximum brightness temperature coupled with emissivity equal to 1 and minimum brightness temperature coupled with lowest emissivity ε_{\min} :

$$\begin{aligned} 1 &= p \max(T_{b_i}) + q, \\ \varepsilon_{\min} &= p \min(T_{b_i}) + q. \end{aligned} \quad (3.4)$$

The next step is estimation of the the lowest emissivity ε_{\min} .

This is done by varying ε_{\min} over the range of possible emissivities for natural materials $[0.6, 1]$, determining corresponding coefficients p and q by solving (3.4) and then approximating emissivity by (3.3) using brightness temperature for all spectral bands. The estimated emissivity is then used together with land-leaving radiance L_{LL} and down-welling radiance L^\downarrow in a computation that yields spectral radiance:

$$L'_i = \frac{L_{LL_i} - (1 - \varepsilon_i)L_i^\downarrow}{\varepsilon_i}. \quad (3.5)$$

The temperature in every spectral band is derived from spectral radiance L' applying inverse Plank's law. The highest one is chosen as the reference temperature T_{\max} . Finally, the estimated spectral radiance L' and Planck's law at the reference temperature T_{\max} are normalized and compared against each other as follows:

$$\sum_i \left| \frac{B_i(T_{\max})}{\|B(T_{\max})\|_1} - \frac{L'_i}{\|L'\|_1} \right|.$$

The value of ε_{\min} is considered final if its corresponding spectral radiance L' is the best fit to Plank's law.

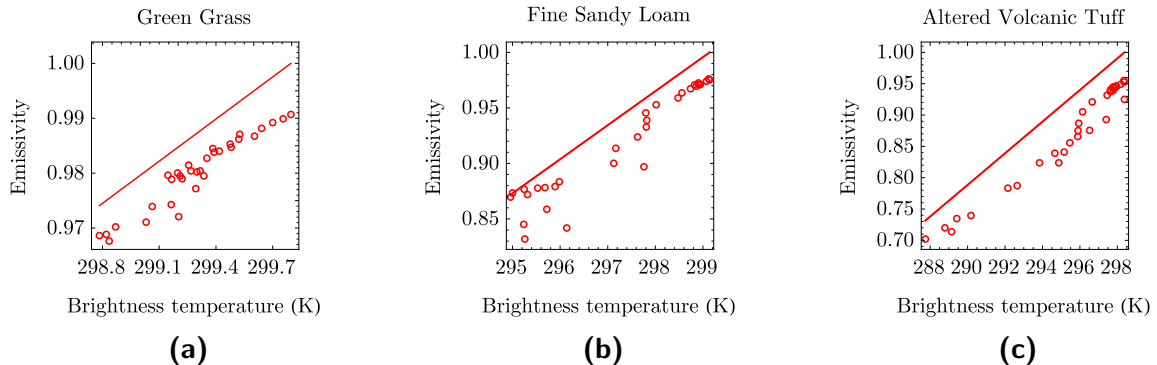


Figure 3.3: Symbols represent examples of the relationship between brightness temperature T_b and emissivity as would be observed by TASI sensor. Lines illustrate the approximations of the relationship between brightness temperature and emissivity. The procedure used for estimation of the brightness temperature and emissivity relationship is described in text.

The whole process of determining ε_{\min} can be understood as smoothing the spectrum by finding the optimal value of ε_{\min} . Pseudocode depicted in Figure 3.4 summarizes the above described procedure as a function $\text{SMOOTHINGERR}(\varepsilon_{\min}, L_{LL}, L^{\downarrow})$ evaluating the error between Planck's law and estimated spectral radiance. This function is minimized with respect to the variable ε_{\min} as follows:

$$\arg \min_{\varepsilon_{\min} \in [0.6, 1]} \text{SMOOTHINGERR}(\varepsilon_{\min}, L_{\text{LL}}, L^{\downarrow}).$$

Continuous curves in Figure 3.3 show the optimal brightness temperature and emissivity relationship approximation. Let us emphasize that by applying emissivities obtained from the approximated relationship between brightness temperature and emissivity to (3.5), one gets L' as the best fit to Planck's law. This means that $B^{-1}(L'_i)$ produces a temperature value for each band. These temperatures have minimum variability since they are derived from the best fit to Planck's law. Let us also remind the reader that maximum brightness temperature is coupled with emissivity equal to 1, which implies that it is part of the set of temperatures with smallest variability. It is important to note that maximum brightness temperature T_b computed from land-leaving radiance is usually smaller than surface temperature T computed from surface radiance. Land-leaving radiance is smaller than surface radiance since natural materials are of emissivity higher than 0.6 and the contribution from reflected downwelling radiance is usually much lower than surface radiance. By reason of maximum brightness temperature T_b being smaller than surface temperature T and by being part of the set of temperatures with smallest variability, it can be concluded that maximum temperature from the set of temperatures tends to be the closest to the surface temperature T and is therefore taken as the reference one.

Before passing emissivity to the Ratio and MMD modules, it is recomputed according to the following equation:

$$\varepsilon_i = \frac{L_{\text{LL}i} - L_i^\downarrow}{B_i(T) - L_i^\downarrow}, \quad (3.6)$$

where T is the maximum temperature associated with optimal ε_{\min} . Equation (3.6) is derived from (3.1) and it is important for relating temperature and emissivity. This

Function SMOOTHINGERR($\varepsilon_{\min}, L_{LL}, L^\downarrow$)
1. $T_{bi} = B^{-1}(L_{LL_i})$
2. Find p and q by solving
$1 = p \max(T_{bi}) + q$
$\varepsilon_{\min} = p \min(T_{bi}) + q$
3. Estimate emissivity
$\varepsilon_i = p T_{bi} + q$
4. Estimate spectrum
$L'_i = \frac{L_{LL_i} - (1 - \varepsilon_i)L_i^\downarrow}{\varepsilon_i}$
5. $T_{\max} = \max(B^{-1}(L'_i))$
6. return
$\sum_i \left \frac{B_i(T_{\max})}{\ B(T_{\max})\ _1} - \frac{L'_i}{\ L'\ _1} \right $

Figure 3.4: Pseudocode of the function that is being minimized in order to estimate the value of ε_{\min} .

recomputation keeps temperature and emissivity consistent with each other (i.e. the same temperature can be derived from any emissivity band). The emissivity is then further processed with the Ratio and MMD modules, with minor changes to the original version of the TES algorithm as it is described in [20] and [21]. These changes include: 1) there is no refinement of ε_{\max} according to the emissivity spectral contrast, 2) the threshold T_1 for separation emissivities with small spectral contrast is not applied, and 3) the number of MMD iterations is set to one. Let us emphasize that before reporting algorithm outputs, emissivity is recomputed by (3.6) using the final value of temperature.

4

OSTES Validation

The OSTES algorithm was tested on both synthetic and real data. Synthetic data were generated from spectral and climatological libraries such that they cover many possible scenes and conditions. These data were simulated as would be acquired with ASTER, AHS and TASI sensor. For OSTES validation on real data were used ASTER image data over Lake Baikal and Caspian Sea, and TASI image data over city of Brno.

4.1. Synthetic Data

Imaging Systems

Synthetic data are intended to cover many possible situations of acquiring thermal data. Therefore three different sensor architectures were chosen to test the OSTES algorithm and compare the results with the TES algorithm.

From the wide range of airborne sensors operating in the TIR region two are chosen as examples: AHS operated by Spanish Institute of Aeronaedics (INTA) and developed by ArgonST (Fairfax, USA), and TASI sensor. These sensors offer data of great importance in applications. Notable studies include areas of mineral mapping [43], soil moisture estimation [53], urban studies [58], soil organic carbon estimation [44] and crop water stress characterization [45], among others.

The above-mentioned airborne sensors were chosen together with the ASTER sensor to analyze the performance of the OSTES algorithm. ASTER consists of 15 bands of which 5 are situated in TIR region with Noise Equivalent Temperature difference ($NE\Delta T$) ≈ 0.3 K. The spatial resolution of the TIR bands is 90 m. The AHS sensor has been fully operational from 2005 [14]. Its sensor operates in 80 spectral bands where the last 10 bands cover atmospheric window from 8 to 13 μm [56]. The AHS TIR bands have a Full Width at Half Maximum (FWHM) ≈ 0.5 μm with $NE\Delta T \approx 0.5$ K. The third sensor we will consider is TASI sensor. It contains 32 bands all of which are in the TIR region. Bands are situated in the 8 to 11.5 μm region and have a FWHM ≈ 0.11 μm with $NE\Delta T \approx 0.1$ K. The response functions of these sensors are depicted in Fig. 4.1.

Data Set

A data set of 6588 samples was artificially created to compare the performance of the TES and OSTES algorithms. Samples include 108 different natural surfaces chosen from

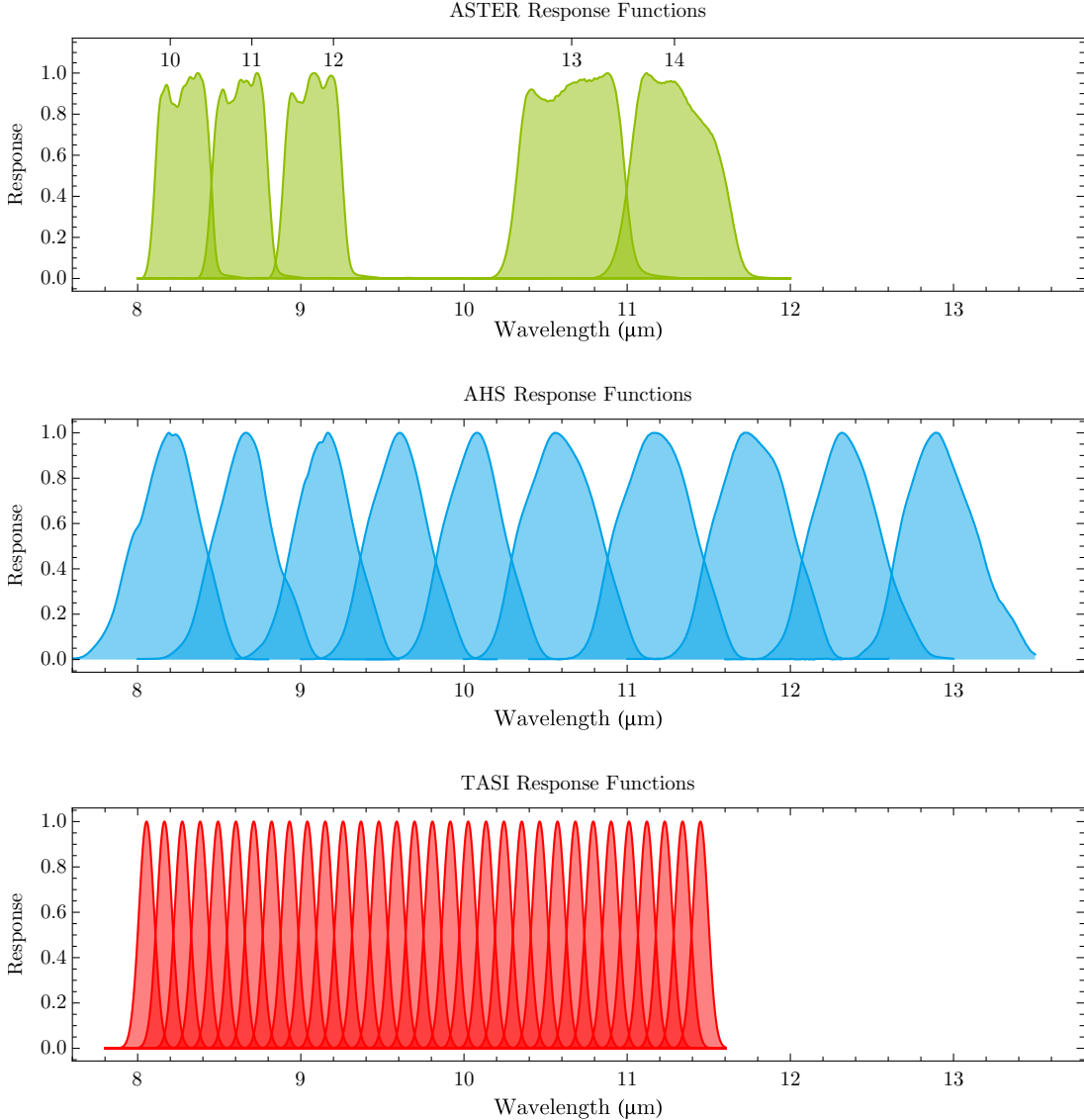


Figure 4.1: Response functions for ASTER, AHS and TASI sensors. The ASTER Band Numbers are shown above the ASTER response functions.

ASTER spectral library [2] at different temperatures coupled with 61 different atmospheric conditions taken from TIGR (TOVS Initial Guess Retrieval) database [10, 9]. Sample temperatures range from 244 K to 310 K. In order to simulate real conditions, every sample at certain temperature is coupled with certain type of atmosphere. The chosen atmospheres represent a variety of possible conditions within polar, mid-latitude and tropical airmasses. These samples were processed to land-leaving and downwelling radiance, as standard TES algorithm input, and they were transformed to band-effective quantities with respect to the ASTER, AHS and TASI response functions. Samples were passed to the algorithms individually.

Simulated data for the ASTER sensor were processed with the current implementation of TES, as it is used for generation of ASTER standard products AST_05 and AST_08 [1]. The version of the original TES algorithm in cases of AHS and TASI sensors was implemented in a manner similar to that described in [35]. In addition, the implementation

Sensor	a	b	c	r^2
ASTER	0.994	-0.687	0.737	0.983
AHS	1.000	-0.782	0.817	0.994
TASI	1.001	-0.737	0.760	0.997

Table 4.1: Regression coefficients of $\varepsilon_{\min} = a + b \text{MMD}^c$ and coefficients of determination r^2 .

omits the ε_{\max} refinement for emissivities with low spectral contrast. The OSTES was applied to all sensors as it is described in section 3.2.

Let us remind the reader that the regression coefficients in 3.2 needs to be refined for each sensor with respect to its response functions. The regression coefficients in (3.2) were recomputed for AHS and TASI sensors using their respective response functions. In both cases the regression was performed on a set of 108 spectra chosen from same categories and library as in the ASTER case. The coefficients for different sensors are shown in Table 4.1.

Validation

Samples were passed to the TES and OSTES algorithms and the temperature and emissivity results were compared with true values. We divide the results into two groups according to the emissivity spectral contrast. For each sensor type we determined a threshold for Maximum-Minimum emissivity Difference (MMD) in order to separate the samples with small spectral contrast such as water, vegetation, snow or samples with small particle sizes from other samples with higher spectral contrast. The threshold was determined for each sensor separately since different response functions and spectral ranges result in different MMD values for the same sample. The performance of both TES versions was determined by subtracting retrieved temperature from true temperature value. The temperature error and chosen MMD values for ASTER, AHS and TASI are shown in Fig. 4.2.

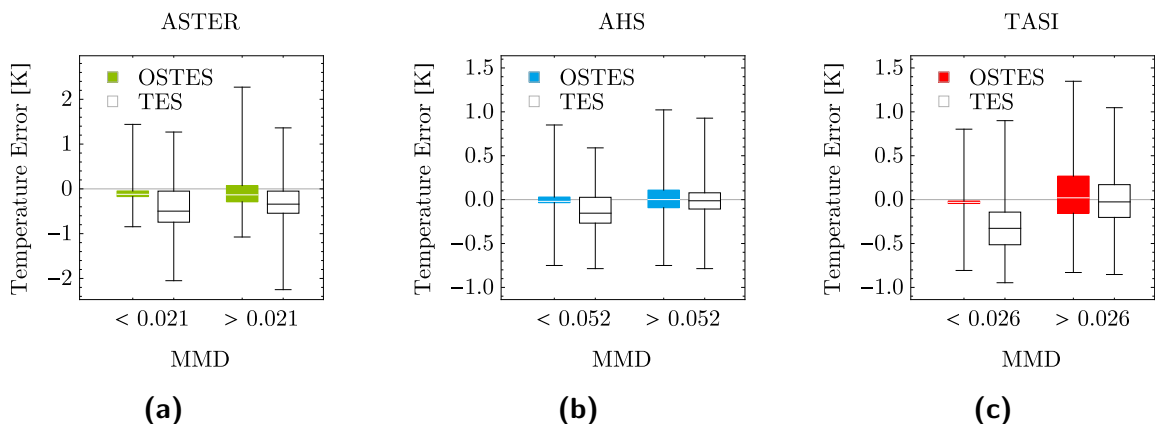


Figure 4.2: Box plots representing temperature error produced by OSTES and TES algorithm for ASTER, AHS and TASI sensor. Results are divided in two groups based on the Maximum-Minimum emissivity Difference (MMD) in order to demonstrate the improvement of the OSTES algorithm. Whiskers represent minimum and maximum of temperature error.

Sensor	MMD	OSTES	TES
ASTER	< 0.021	0.25	0.50
	> 0.021	0.36	0.43
AHS	< 0.052	0.13	0.20
	> 0.052	0.20	0.19
TASI	< 0.026	0.16	0.32
	> 0.026	0.32	0.30

Table 4.2: Standard deviations of temperature errors obtained by applying OSTES and TES algorithm on simulated data as seen by ASTER, AHS and TASI grouped according to the sample Maximum-Minimum emissivity Difference (MMD).

It can be seen that temperature and emissivity retrieved with OSTES are more accurate for samples with low spectral contrast. On the other hand, no significant improvement is evident in cases of samples with higher spectral contrast.

Let us remind the reader that every sample is processed under several different atmospheric conditions coupled with different sample temperatures. Thus the standard deviation of temperature and emissivity error is indicative of the algorithm's sensitivity to seasonal fluctuations. A comparison of standard deviations of temperature errors introduced by both TES approaches reveals that the OSTES is less sensitive to changes in atmosphere and sample temperature for samples with low MMD. However, the standard deviations of temperature errors of samples with higher MMD are similar. Standard deviations of temperature errors obtained by the OSTES and TES algorithms are summarized in the Table 4.2.

4.2. Real Data

The OSTES temperature and emissivity were firstly compared with ASTER standard products AST_08 (kinetic temperature) and AST_05 (surface emissivity). For this purpose were chosen scenes containing water bodies. Water emissivity is well-known and does not vary significantly which offers a unique opportunity for testing various algorithm features. Water bodies are commonly used for calibration [64, 61] and validation [63] [62] purposes. Secondly was OSTES applied on image data acquired by TASI sensor and the results were compared with emissivities obtained from *in-situ* measurements and TES emissivity retrievals.

Comparison with ASTER standard products

The performance of the OSTES algortihm was also tested and compared with standard ASTER products. Testing is focused on: 1) investigating the impact of seasonal changes on emissivity retrievals, and 2) emissivity smoothness over homogeneous areas. Both tasks were performed on ASTER scenes containing large water bodies. For the first task we chose five scenes of the Caspian Sea acquired in various seasons of the year. For the second task we chose Lake Baikal. The list of all scenes used, together with their acquisition and processing date is given in Table 4.3. For every scene we downloaded

Location	Acq date	Processing date
Caspian Sea	11.02.2001 - 07:35:55 (UTC)	19.11.2015
Caspian Sea	30.09.2001 - 07:35:57 (UTC)	19.11.2015
Caspian Sea	29.06.2002 - 07:31:47 (UTC)	19.11.2015
Caspian Sea	21.08.2004 - 07:29:35 (UTC)	19.11.2015
Caspian Sea	13.11.2008 - 07:24:21 (UTC)	19.11.2015
Lake Baikal	22.07.2002 - 04:17:29 (UTC)	27.08.2015

Table 4.3: ASTER scenes used for algorithm testing

ASTER standard products AST_09T, AST_08 and AST_05 delivering land-leaving and downwelling radiances, surface kinetic temperature and surface emissivity, respectively. Product AST_09T was used as input to the OSTES algorithm. The resulting temperature and emissivity was then compared with the AST_08 and AST_05 standard products. The emissivity variability over large and homogeneous area was chosen to be the quality indicator, since we are interested in the retrieval of material properties, which should be constant within the time and space.

From the Caspian Sea scenes we chose samples of size 40×40 pixels over uniform, cloudless waterbody. These subsets were processed by the OSTES algorithm and the emissivity results were averaged for every scene. The results are plotted in Fig. 4.3 along with the emissivities that were delivered in the AST_05 product and averaged over the same spatial subset. In most cases the AST_05 emissivity spectra appear to be closer to the sea water emissivity spectra taken from ASTER spectral library [2]. However, the temperature retrievals of extracted samples obtained by OSTES and TES are very close (not shown). The average temperature difference of AST_08 and OSTES results computed from all Caspian Sea samples is 0.2 K (s.d. 0.2 K). The fact that the temperatures obtained with the two algorithms are very close, but the emissivities are not implies that the emissivity spectra from AST_05 product are not consistent with temperature from AST_08 product. We verified this inconsistency by taking the temperatures delivered in AST_08 and the downwelling and land-leaving radiances delivered in AST_09T and putting these into (3.6) to obtain emissivities that are different from what is in the AST_05 product. These emissivity spectra derived from AST_08 and AST_09T, which we refer to as “recomputed emissivities”, are depicted on Fig. 4.3 as well. Comparing recomputed emissivity spectra and OSTES results shows that in scenes acquired on 29.6.2002 and 30.9.2001 are results similar. On the other hand OSTES results perform slightly better in scenes acquired on 11.2.2001, 21.8.2004 and 13.11.2008. Nevertheless, none of the emissivity spectra agrees with expected values.

The difference in emissivity obtained by the two versions of TES is further illustrated in the scene over Lake Baikal shown in Fig. 4.4. In this figure the white squares on the images define a water body sample of size 90×90 pixels that was used to produce the values in the histograms below the images. The expected values of sea water emissivity (red vertical line) are included in the Fig. 4.4. The histograms show the OSTES emissivity retrievals compared against the AST_05 standard product, as well as the emissivity recomputed with respect to the temperature delivered by AST_08 and land-leaving and downwelling radiance delivered by AST_09T, as described in the previous paragraph. Inspection of the ASTER standard product AST_05 shows step discontinuities in bands 10, 11 and 12

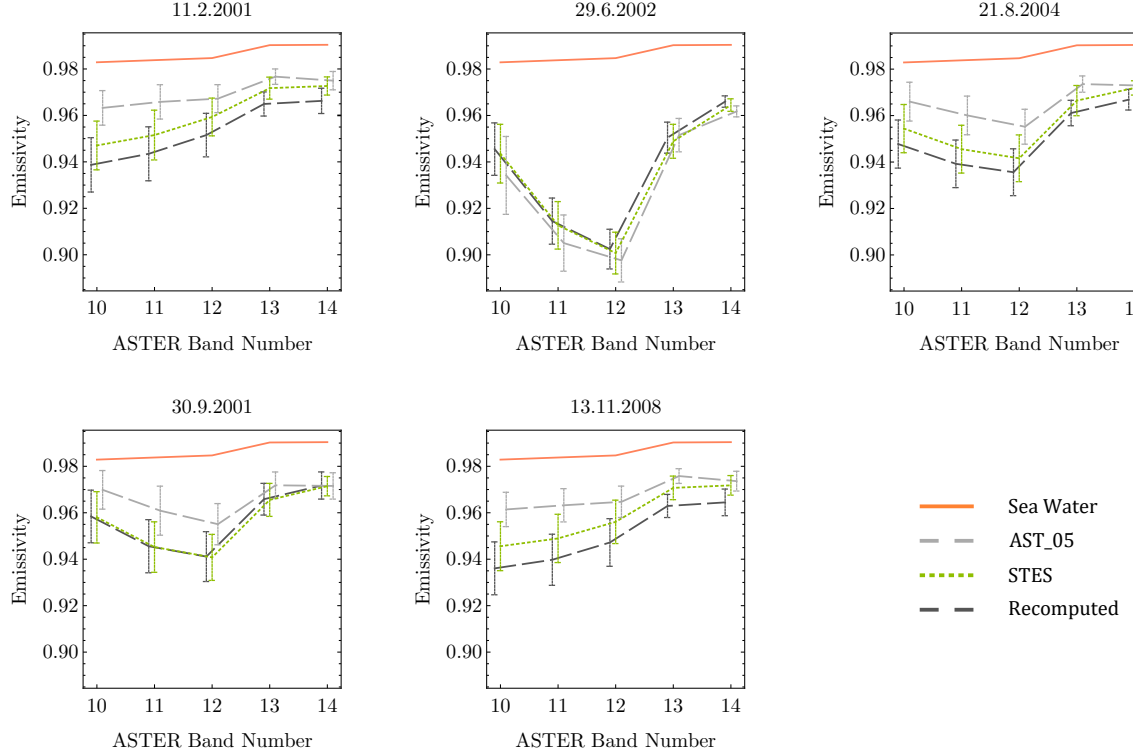


Figure 4.3: Emissivity of Caspian Sea in different seasons obtained from ASTER standard product AST_05, OSTES retrieval, and emissivity recomputation according to the temperature from AST_08 and land-leaving and downwelling radiance from AST_09T. Emissivities were extracted from area of size 40×40 pixels over pure and cloudless waterbody. Error bars display standard deviation.

over the study sample, which is reflected in the bimodal distributions in the histograms and the noisy patterns in the left image. On the contrary, OSTES emissivity results are smoother and the histograms do not show any significant discontinuities. The recomputed and OSTES emissivity retrievals are similar. However, the OSTES emissivities tend to be closer to the expected values. In addition to the noise, striping is also visible in the image. This is not consequence of the TES algorithm and is more deeply discussed in [19]. Even though the AST_05 and OSTES emissivities differ significantly in some bands, the temperature retrievals are very similar. The average difference is 0.25 K (s.d. 0.18 K). Similar to the discussion regarding Caspian Sea emissivity retrievals, it can also be concluded in this case that none of the emissivity spectra have satisfying values.

The discrepancies in shape and magnitude of emissivity spectra can be caused by various source of errors but the main error source has been attributed to imperfect atmospheric corrections. The impact of this error is evident mainly in cases of low spectral contrast. Notable works discussing emissivity retrievals with low spectral contrast are [62, 63, 64, 13, 54]. One suggested improvement is the water vapour scaling method [61, 19].

The step discontinuities in emissivity values over homogeneous area can occur due to various thresholds deciding how to treat the sample during processing. The original TES algorithm starts in the NEM module assuming a maximum emissivity spectra $\varepsilon_{\max} = 0.99$. The NEM module is then restarted with refined ε_{\max} according to the emissivity retrieved from the first NEM pass. Also, temperature and emissivity from NEM are reported as the

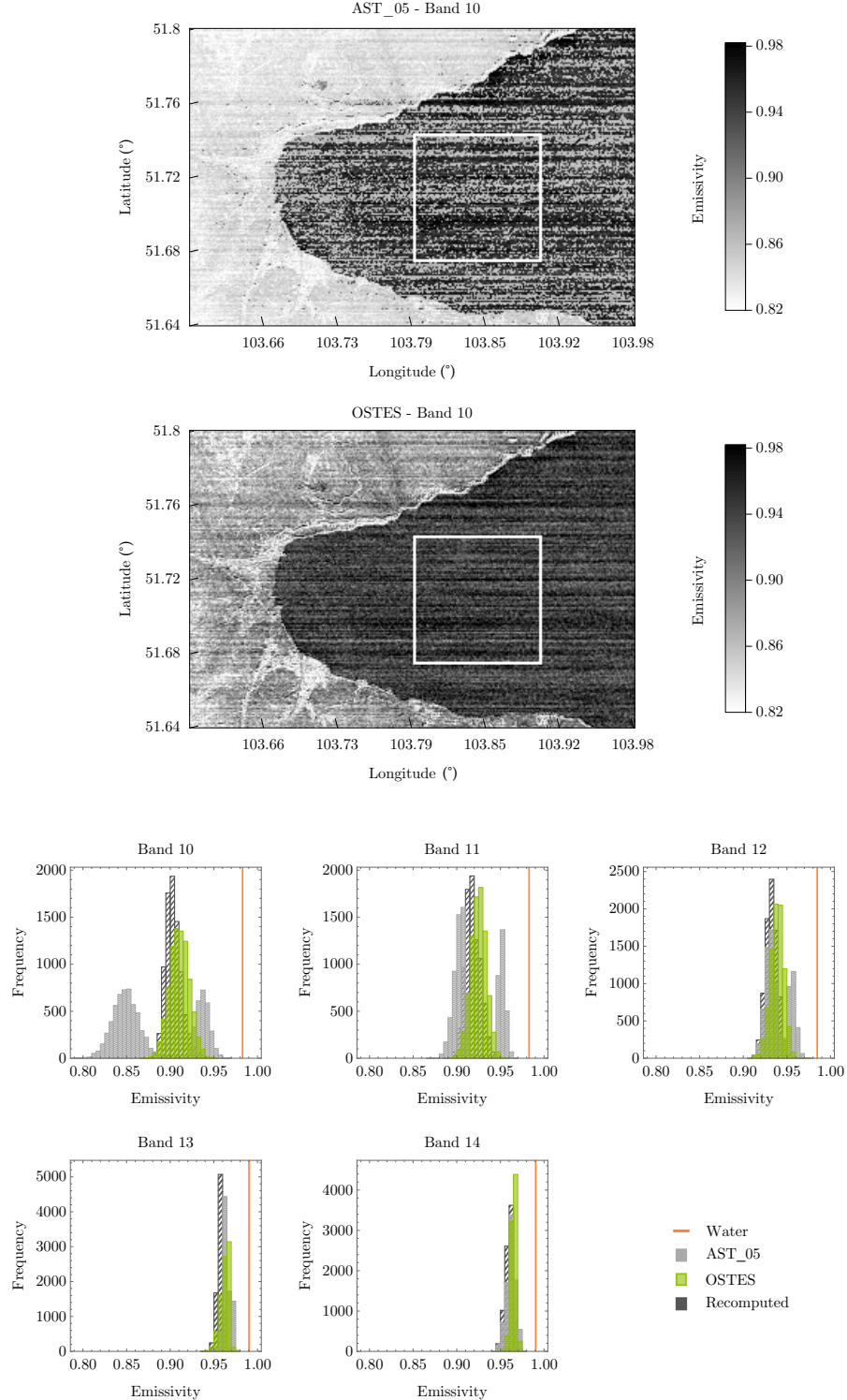


Figure 4.4: ASTER band 10 emissivity images of Lake Baikal obtained from ASTER standard product AST_05 (upper left) and OSTES emissivity retrieval (upper right). In both images the same contrast stretching is used. The white square represents the area from which emissivity histograms were created (lower panel). Histograms show distributions of AST_05 emissivity, OSTES emissivity and recomputed emissivity according to the temperature from AST_08 and land-leaving and downwelling radiance from AST_09T. Line depicted in histograms indicates the expected value of water emissivity retrieved from ASTER spectral library [2].

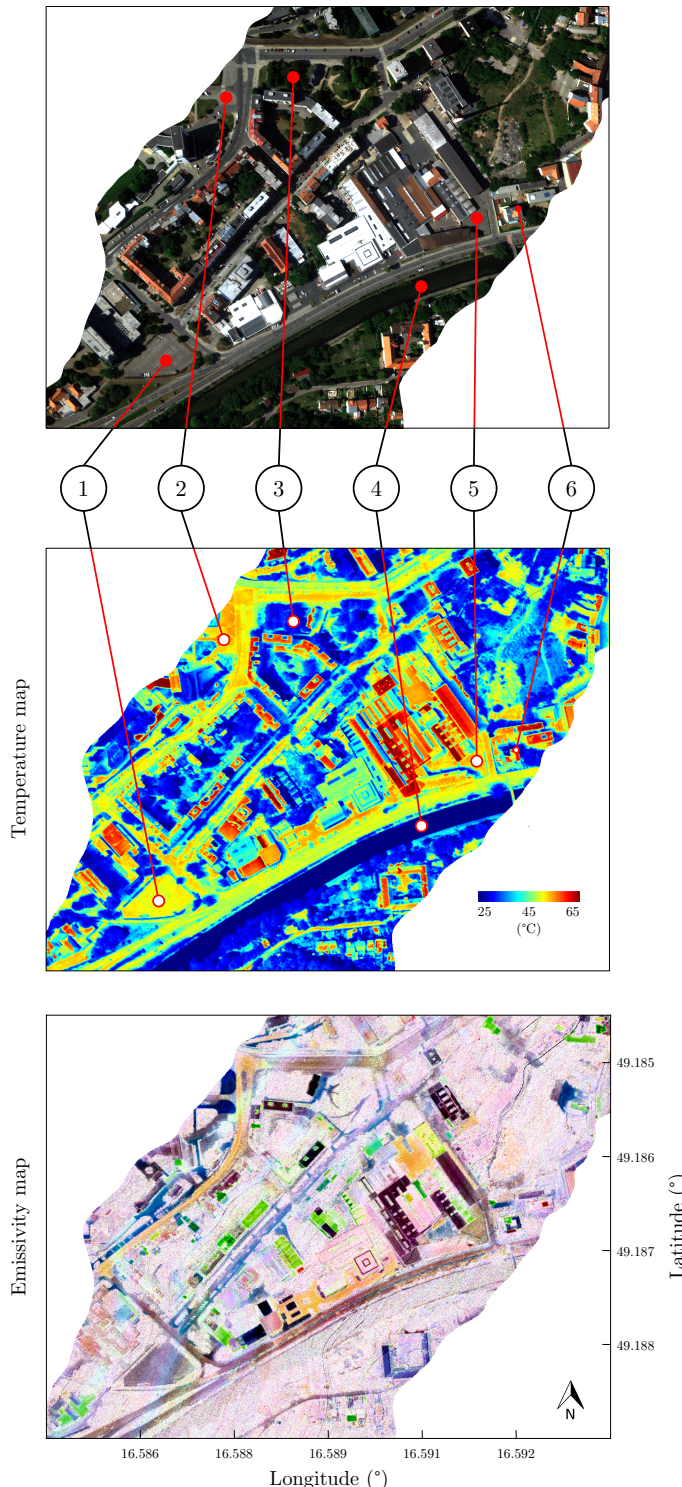


Figure 4.5: Part of flight line over the city of Brno. Image data were acquired on 4.7.2015 at 14:03 (UTC). The top image displays RGB composition of the studied area. The middle image depicts temperature map obtained from OSTES algorithm applied on image data from TASI sensor. The bottom image is false color emissivity map obtained from OSTES algorithm (red - band 10, green - band 15, blue - band 20). On the top and middle images are shown locations and labels *in-situ* measurements.

result of TES algorithm if the correction for downwelling radiance is not possible. The original version of TES processes samples according to the MMD of emissivity spectra obtained from NEM module either by incorporating (3.2) or by presetting emissivity to $\varepsilon = 0.983$. Some authors [23], [49] have suggested that the value of the threshold used for classifying observations into groups with either low or high spectral contrast should be changed or completely removed. Observations with wrongly determined spectral contrast or observations with spectral contrast close to any threshold result in step discontinuities. On the contrary, the OSTES does not set any thresholds for materials with low spectral contrast and so it is expected to generate smoother results on homogeneous areas with low spectral contrast.

Application to TASI Image Data

The study was performed using data acquired over the city of Brno, Czech Republic (lat: 49.2, lon: 16.6). The data examined come subset of one flight line crossing the city from south-west to north-east. The acquisition was performed on 4.7.2015 at 14:03 (UTC). The FLIS operated by Global Change Research Institute CAS (Brno, Czech Republic) [24] was used for this acquisition. FLIS consists of Compact Airborne Spectrographic Imager (CASI), Shortwave infrared Airborne Spectrographic Imager (SASI) and TASI sensor. All sensors are developed by Itres Ltd. (Calgary, Canada). Image data acquired by CASI, SASI and TASI sensor were radiometrically and atmospherically pre-processed, and geo-orthoreferenced to UTM coordinate system.

Within this study were performed *in-situ* measurements of urban materials with Fourier transform infrared (FTIR) Spectrometer Models 102 developed by D&P Instruments (Simsbury, USA). The emissivity of measured surfaces was estimated by a spectral smoothing algorithm [27]. Emissivity spectra of water and deciduous trees were not measured but instead they were extracted from ASTER spectral library [2]. All emissivity spectra were resampled with respect to TASI response functions. The study area and locations of the *in-situ* measurements are shown in the upper part of the Figure 4.5.

The processing of image data acquired by TASI was limited to 22 spectral bands. First five and last five spectral bands were not considered since they were affected by imperfect atmospheric corrections. Temperature and emissivity results of the OSTES algorithm are depicted in the middle and lower part of Figure 4.5 in the form of temperature and emissivity map. Temperature map shows high temperature differences between vegetated and built areas. Emissivity map is false color composition (red - band 10, green - band 15, blue - band 20) showing variability of surface materials in the image.

In-situ measurements were not performed during the overflight. Therefore temperature could not be used for comparison and validation of the TES and OSTES algorithms. The comparison of the TES and the OSTES algorithms' performance was tested against six emissivities obtained from *in-situ* measurements. Results are shown in Fig. 4.6 below, where error bars display standard deviation. Both TES and OSTES emissivity retrievals are very similar. The OSTES performs slightly better than TES in cases of deciduous trees and Svatka River. However, none of these two spectra agrees with the shape and magnitude of expected emissivity spectra. These discrepancies can be caused by various sources of errors but the main error source has been attributed to imperfect atmospheric corrections. Emissivities of spot 5, asphalt parking lots, retrieved by the TES and OSTES significantly differ from *in-situ* measurement. This shift in magnitude is introduced by

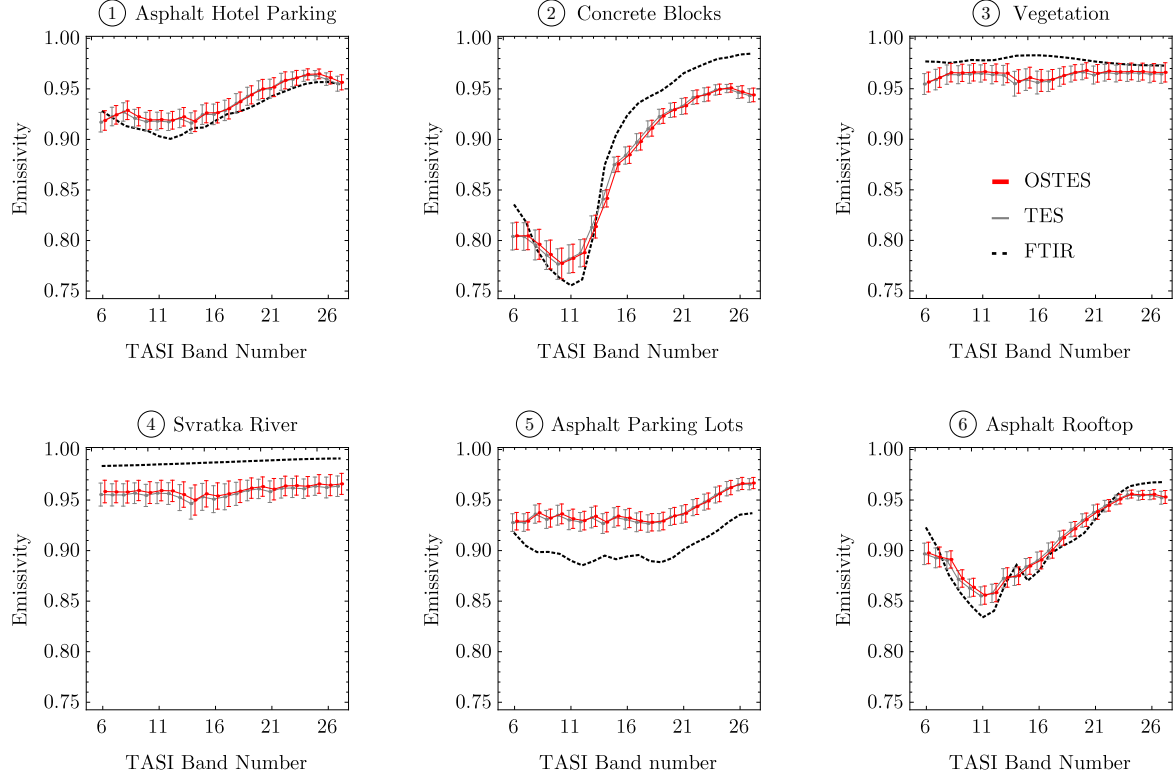


Figure 4.6: Comparison of TES and OSTES emissivity retrievals with emissivities obtained from *in-situ* measurements.

insufficient compensation of downwelling radiance. This spot is surrounded by buildings, which increase the amount of downwelling radiance. This additional radiance is not included in atmospheric parameters retrieved from MODTRAN. The rest of the emissivity retrievals are considered to follow *in-situ* measurements well. Let us emphasize the reader that OSTES offers only moderate improvements in emissivity retrievals. These are not possible to observe in this comparison due to the magnitude of error introduced by imperfect atmospheric corrections.

These data were acquired within a campaign focused on detecting urban heat island of the city of Brno. The main goal were determination of parameters affecting temperatures in the city. Preliminary observations are introduced in the Appendix A.

5

Ground Measurements

5.1. Introduction

Post-mining sites represent areas of large-scale and intensive disturbance. They have serious impact on the surrounding landscape in many countries of the world. Original ecosystems are destroyed, and the restoration of ecosystem functions and services is necessary [8]. Afforestation is widely used reclamation method. Many studies demonstrate that post-mining sites have a large potential for carbon sequestration if afforestation has been applied [67, 16, 51, 65]. This can contribute to mitigate the increase in atmospheric CO₂ concentrations.

During opencast mining a large amount of substrate above the coal layer is removed and relocated in heaps covering extensive areas. These heaps consist of material often excavated from depths of several hundred meters. This material is called spoil substrate and it can vary in its physical and chemical properties. The heterogeneity is largely affected by geology and the method of mining and heaping. For this reason the substrates differ substantially from recent soils. They often have extreme pH and may contain high concentrations of heavy metals, polyphenols (i.e., products of coal decomposition) and salt content. Such properties can significantly impact a success and/or speed of vegetation development at post mining sites. Therefore a proper knowledge on spoil substrate properties and distribution is necessary in land rehabilitation.

Thermal remote sensing can provide beneficial tools for monitoring of post-mining areas. Particularly, land surface emissivity (LSE) can be used for spoil substrates classification. In addition, physical and chemical properties can be estimated by spectral analysis of LSE. Land surface temperature (LST) is closely connected to soil moisture which is important for establishment of new ecosystems.

LST is coupled with LSE and thus one quantity cannot be derived without knowledge of the second. These quantities cannot be explicitly derived from radiance measurement. The reason is that by observing radiance in N bands one gets N unknown emissivities plus one unknown temperature. Such a system of equations is underdetermined (i.e., more unknown than known variables). Several algorithms have been suggested to solve this problem [40]. These algorithms either require knowledge of LSE in advance, or an estimate LSE as a part of their output. A library of spectral emissivities can be utilized for: 1) determination of LST, 2) material classification, and 3) LSE validation of airborne and satellite thermal remote sensing data.

This work describes a spectral library of spoil substrate emissivities from brown coal mining sites in the Czech Republic near towns of Sokolov, Chodov, Bílina and Ustí nad

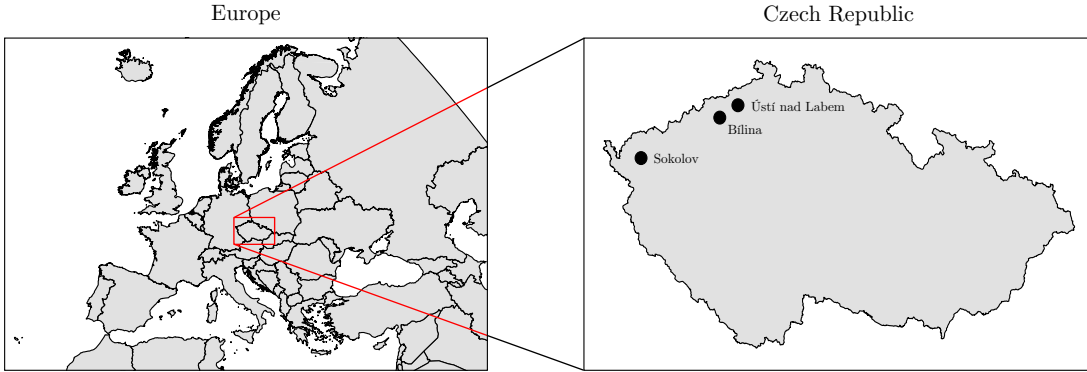


Figure 5.1: Locations of brown coal mining sites from which spoil substrate samples were extracted.

Labem (Fig. 5.1). The spectral library contains emissivities, soil pH in water and in KCl, soil conductivity, content of water soluble Na and K, Al and Fe in KCl, loss on ignition and content of polyphenols. In addition to all measured physical and chemical parameters, sample's latitude and longitude are listed. The dataset consists of 24 spoil substrate samples, which were homogenized by mixing and sieving before any sample analysis. The toxicity test and measurement of chemical properties are discussed at length in [15]. Data collection for emissivity retrievals was performed outdoors in Petri dishes using a Fourier transform infrared (FTIR) spectrometer Model 102 (D&P Instruments, United States). The emissivity of each sample was estimated by a spectral smoothing algorithm [27].

Datasets containing LSE are rare in comparison with datasets containing LST measurements. The most well-known spectral libraries containing emissivities are the ASTER Spectral Library [2], Johns Hopkins University Spectral Library [50], Arizona State University Spectral Library [11], United States Geological Survey Spectral Library [12] and the Spectral Library of Urban Materials (SLUM) [39]. However, these spectral libraries do not include neither geographical coordinates of samples nor representatives of spoil substrates. One example of a spectral library of emissivities from calibration/validation sites containing coordinates for each sample is described in [57]. The dataset described in this paper is exceptional in its nature and location.

The data presented in this paper were used in a study focused on mapping of spoil substrates for site re-cultivation [72] as well as in a study discussing spoil substrates toxicity [15]. The mining site was also mapped with the Airborne Hyperspectral Scanner (AHS) in visible, near infrared, shortwave infrared and longwave infrared regions for mineral classification purposes [43]. Examples of emissivity spectra retrieved from AHS and their corresponding samples spectra extracted from the library are depicted in Fig. 5.2. Samples spectra from the library were spectrally resampled with respect to AHS response functions using weighted averages [40]. Comparison of retrieved spectra in case of samples 11 and 19 shows good agreement in shape. Sample 12 exhibit deviations mainly between bands 3 and 4 (9.24 and 9.68 μm). This can be explained by the fact that AHS pixel has 5x5 m pixel size and these pixels were not pure thus had more complex mineral composition than the collected samples. Discrepancies in magnitude can be addressed to imperfect atmospheric corrections or to different soil state during overflight.

Any activity involving remote sensing over these mining sites can benefit from publicly releasing the spectral library of spoil substrates emissivity. Apart from remote sensing

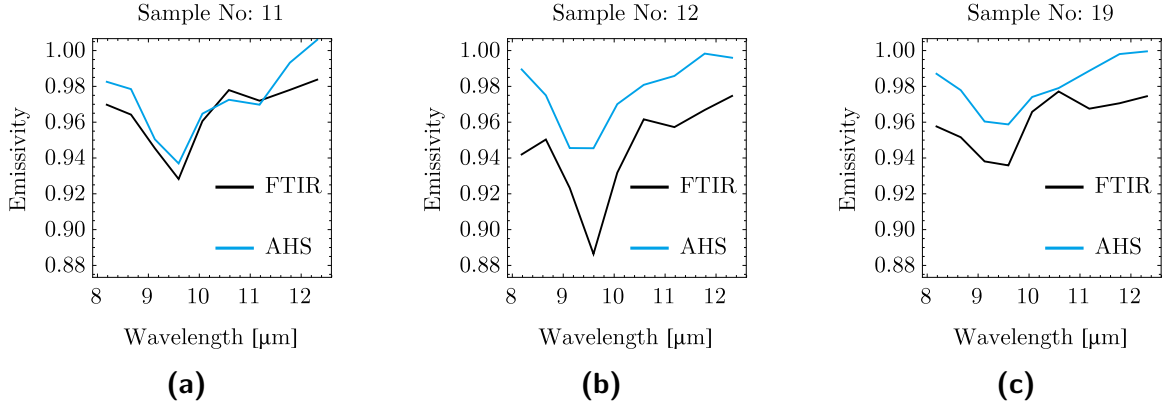


Figure 5.2: Examples of corresponding emissivity spectra retrieved from AHS and from spectral library of spoil substrates'. Emissivity spectra from the library were measured by FTIR and they were resampled with respect to AHS response functions.

application, data in spectral library can be further analyzed for identifying relationships between a sample's spectral emissivity and its chemical properties.

TODO: Data are describe in appendix A and library itself is part supplementary file of article...

5.2. Methods

The study area is situated around two post mining districts: 1) Sokolov – coal-mining district near towns of Sokolov and Chodov (North-West Czech Republic) and 2) North Czech coal mining district near towns of Bílina and Ustí nad Labem (North Czech Republic). Open-pit mines produce large areas of tailings where spoil material was sampled. Claylike tertiary sediments dominate in these districts.

Spoil substrates were sampled from bare soil without vegetation. Samples contained negligible amounts of organic matter. Extracted samples were further homogenized by mixing and sieving through a 2 mm screen. Homogenized samples were divided into two groups, from which the first one was used for chemical analysis and the second one for toxicity testing. Samples set for chemical analysis were air dried and stored in a dark place at room temperature. Soil pH in water and in 1N KCl (which is 74.56 g of potassium chloride diluted in 1000 mL of water [37]) was measured using a pH meter with glass electrode in suspension. The suspension was prepared in 1:5 spoil to water ratio and 1:5 spoil to KCl ratio. Conductivity was measured in filtrated suspension using a conductometer. The suspension was prepared in 1:5 spoil to water ratio. Content of water soluble Na and K was also measured in filtrated water suspension (1:5 spoil to water ratio) using an ion selective electrode. Both suspensions were left to stay overnight. Al and Fe contents in 1N KCl eluate, (1:5 spoil to water ratio), were determined by spectrophotometer Spectra AA 640 (Varian, Australia). Loss on ignition was measured by burning spoil samples at 600 °C for 5 h. This process is called ashing. To determine the amount of polyphenols samples were kept in 80% ethanol (1:5 spoil to ethanol ratio) and stayed for 24 h. Samples were then filtrated and the polyphenol content was determined spectrophotometrically by Folin–Ciocalteau reagent at a wavelength of 765 nm [25]. Gallic acid was used as a standard for calibration. The polyphenol content was expressed as mg/100 g of soil. Toxicity

was determined by enchytraeid toxicity test. The test is based on the population growth of pot worms in substrates. The details of the measurement are discussed in [15].

Spoil substrates emissivity measurements were collected with Designs and Prototypes Model 102 (United States) portable FTIR spectrometer. The measurement was performed outdoor under clear sky conditions during two consecutive days in summer season. The spectroradiometer was pre-heated to maximum expected ambient day temperature during the nights before both measurement days. Spectrometer orientation during measurements was south to avoid shadows. Fore-optics field-of-view was 4.8° and it was 60 cm away from the sample. Such a configuration resulted in spot size of approximately 5 cm. Samples were put in Petri dish of diameter 14 cm and they were let to be heated up naturally by sunlight. Samples temperatures ranged from 40°C to 50°C . Every sample was measured at three different spots. The measurement of one spot consists of ten measurements, which were averaged. The resulting emissivity of each sample is the average of all three measurements. Sample temperature and emissivity were determined by a spectral smoothing algorithm, as described in [27].

During the measurements the instrument was calibrated using two blackbodies at different temperatures. A cold blackbody was set to ambient temperature (30°C) and warm blackbody was set just above the sample temperature ($40 - 50^\circ\text{C}$). The calibration procedure during first four spoil samples was done between the changing of each sample. The calibration procedure during the rest of the measurements was done between every fourth sample. Before every sample a measurement was made of a diffuse gold reflectance plate (Infragold from Labsphere Inc.), to compensate for downwelling radiance, as suggested in [17]. The measurement of one sample along with instrument calibration and measurement of the diffuse gold reflectance plate took around 15 minutes. A description of the procedures for converting instrument response to radiance and compensating for downwelling radiance can be found in [27] and [26].

Some of the spoil substrate emissivity spectra are greater than one at certain wavelengths. This inaccuracy occurs at both ends of provided wavelengths interval (i.e. near $8\ \mu\text{m}$ and near $14\ \mu\text{m}$). Data at these wavelengths are on the edge of atmospheric window and thus the cause of the inaccuracy is imperfect compensation for downwelling radiance. Samples with numbers 33, 34 and 38 are missing header information of latitude and longitude. Absent values are indicated by ‘NA’ string. In these cases the origin of the sample is specified with respect to closest town (either Bílina or Sokolov). We still find these data meaningful, since they can be used as spectral endmembers.

5.3. Data Properties

All samples are claylike sediments which imply that spectral features of clay can be found in every emissivity spectra. Fig. 5.3 depicts three examples of spoil samples taken from the spectral library. Sample 02 (Fig. 5.3a) is clay consisting mostly of kaolinite with significant peaks at 8.90 , 9.50 , and $10.00\ \mu\text{m}$. Sample 06 (Fig. 5.3b) is coal combined with sand and clay. The emissivity spectrum of this sample contains kaolinite features mixed with a quartz feature at 8.50 , 8.90 , 9.30 and $10.00\ \mu\text{m}$. The sample 33 (Fig. 5.3c) is bentonite rich for montmorillonite. Montmorillonite has typical dip in spectral emissivity at $9.43\ \mu\text{m}$. The spectral emissivity library of spoil substrates includes also image providing a preview of all samples in library similar to images shown in Figure 3.

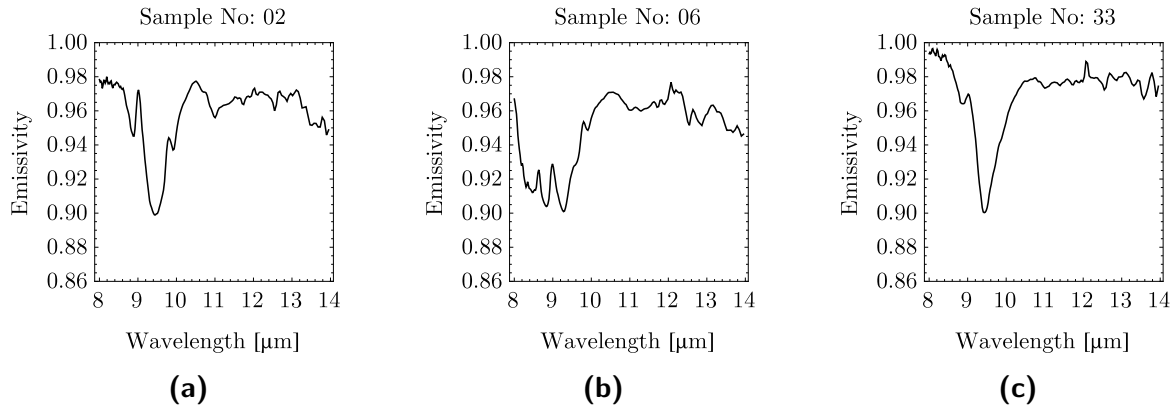


Figure 5.3: Spectra of three samples taken from the spectral emissivity library of spoil substrates: (a) sample 02 representing clay rich for kaolinite; (b) sample 06 representing coal combined with sand and clay; (c) sample 33 representing bentonite.

Thermal remote sensing can be used for classification of spoil substrates and for determination of their physical and chemical properties. The spectral library presented in this paper can ease and enhance all these activities. Obtained information together with LST are valuable for selection and monitoring of restoration process on post-mining sites.

5.4. Spectral Smoothing Algorithm

6

Conclusion

Appendices

A

Dependencies Between City Structure and Thermal Behaviour in Brno

Results of visualisation are presented in Fig. A.1 and Fig. A.2. Both figures have the following structure. A distance along the transect in meters forms a common X axis. A true-colour composition from CASI data is shown in the topmost panel, the transect is drawn with a yellow line. Surface temperatures of a summer day and a summer night are shown in the second panel. Surface temperature of a winter night is shown in the third panel. A depiction of city structure is contained in the fourth panel. Terrain level is shown in brown, while buildings are distinguished from high vegetation with grey and green colours, respectively. NDVI is shown in fifth panel and absorbed energy is shown in the last panel.

Several common observations can be made in both figures. NDVI as a measure of “greenness” follows a classification of high vegetation and also allows distinguishing between streets and a surface covered by grass. Local minima in absorbed energy follow shaded regions at the edges of buildings. Temperature over areas covered by vegetation tends to be more stable and lower in average, while the temperature of streets and parking lots is significantly higher during summer day.

We would like to point out several interesting features in individual transects. We will use an X axis to label the details.

In Figure 1 between 80 and 90, the stabilising role of vegetation can be seen – the temperature profile has a low variability as well as a lower average despite a higher amount of absorbed energy. In Figure 1 at 305 and 390, two different roof surfaces can be observed – the rightmost one is dark, has a high absorptivity, while the leftmost one has a high reflectivity and reflects a cold sky in both summer and winter night. The region from 400 to 550 contains green areas which surrounds Špilberk castle. Summer day temperature is significantly lower in this region compared to other built up areas. The only notable temperature extreme is visible between 460 and 470 where the transect crosses a path walk.

Figure 2 shows interesting features as well. Roofs with high reflectivity can be observed at 160 – 170 and 530 – 540. The coldest places during a summer day are the river between 260 and 280 (which is on the other hand the warmest place in winter) and hard shadows next to high buildings, e.g. at 545. There is a notable shaded hillside between 40 and 50 causing temperature decrease in both summer day and night. There is an interesting dip in the summer night temperature profile between 360 and 370, which is presumably

caused by a parked car in the parking lot. A dip in the summer temperature around 445 is caused by a roof window included in the transect.

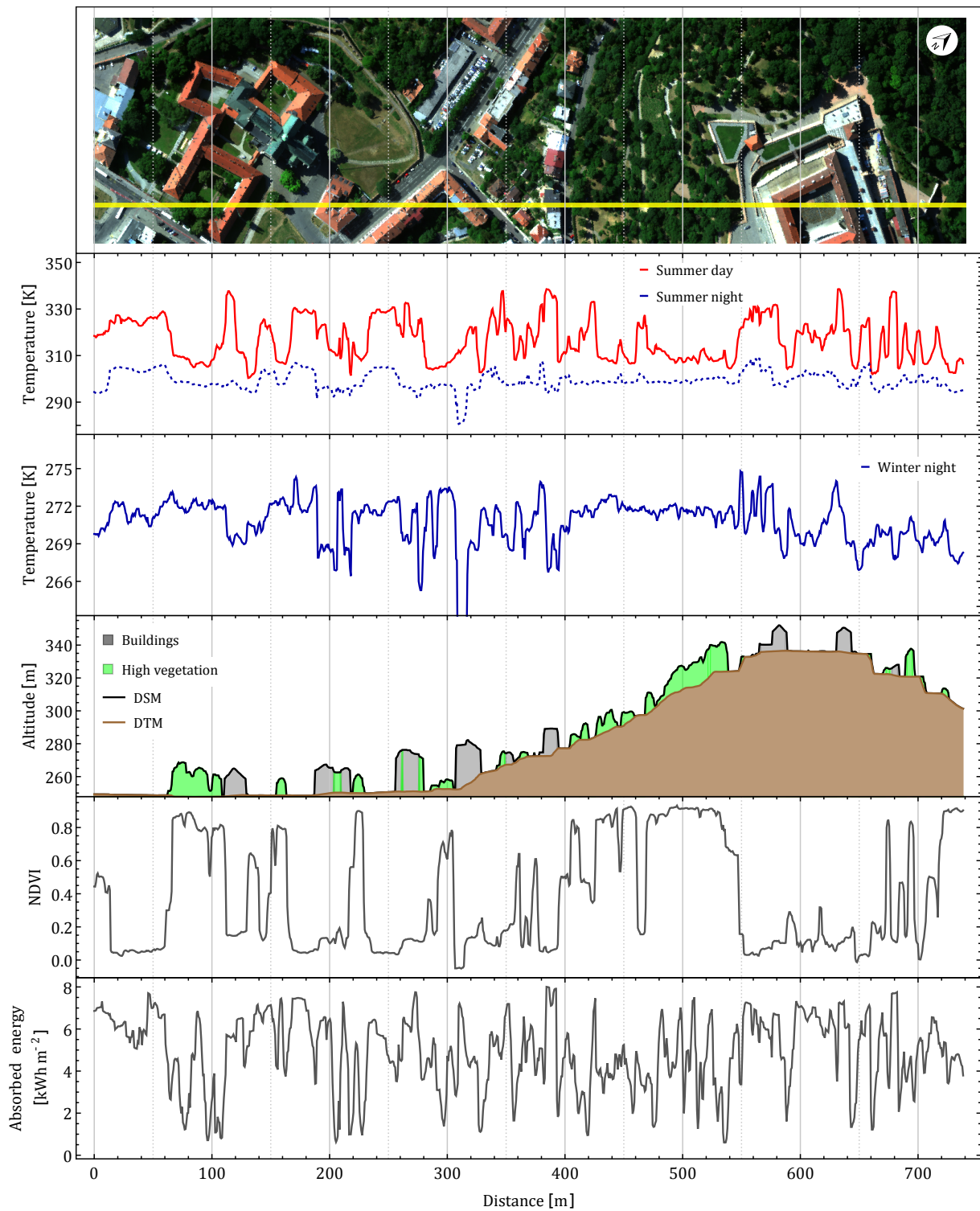
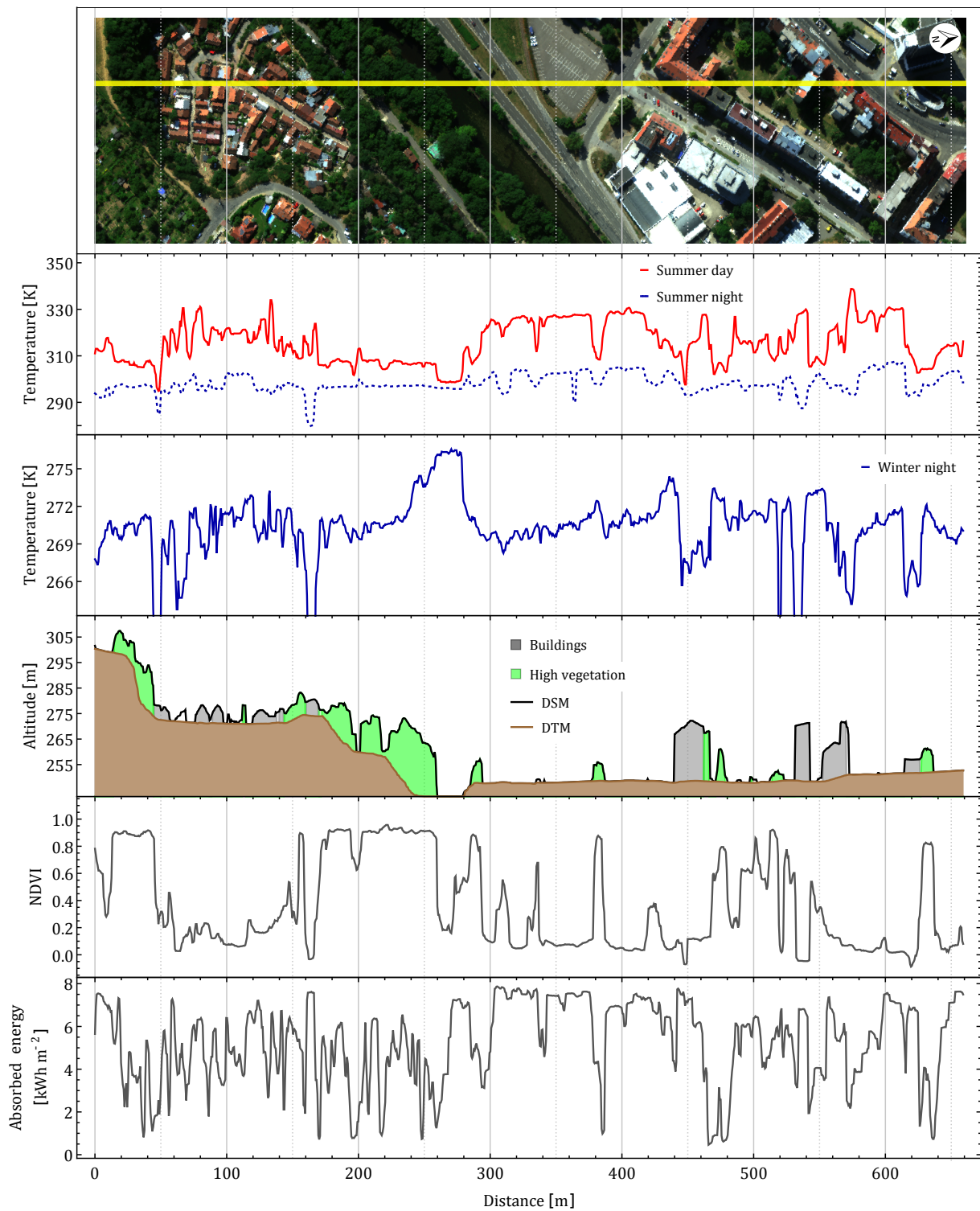


Figure A.1: TODO.


Figure A.2: TODO.

B

Spectral Emissivity Library of Spoil Substrates

The spectral library consists of 24 ASCII files. Each file describes one spoil substrate. Individual files are named according to the sample number. Files consist of a file header and spectral emissivities. Both file parts are described in the subsections below.

B.1. Header

The format of header is similar to format of ASTER Spectral Library header [2]. Each file contains 26 lines of header, which includes available sample information. The header is divided into four sections separated by empty lines. First part contains 9 lines discussing sample classification, particle size and sample origin. Sample origin is expressed by latitude and longitude on the reference ellipsoid WGS84. This information is summarized in the following fields:

1. Name
2. Type
3. Class
4. Particle size
5. Sample No
6. Owner
7. Origin
8. Latitude
9. Longitude

A second section contains information about sample toxicity and chemical properties. The unit of each quantity is indicated in square brackets after quantity name. This header section contains following fields:

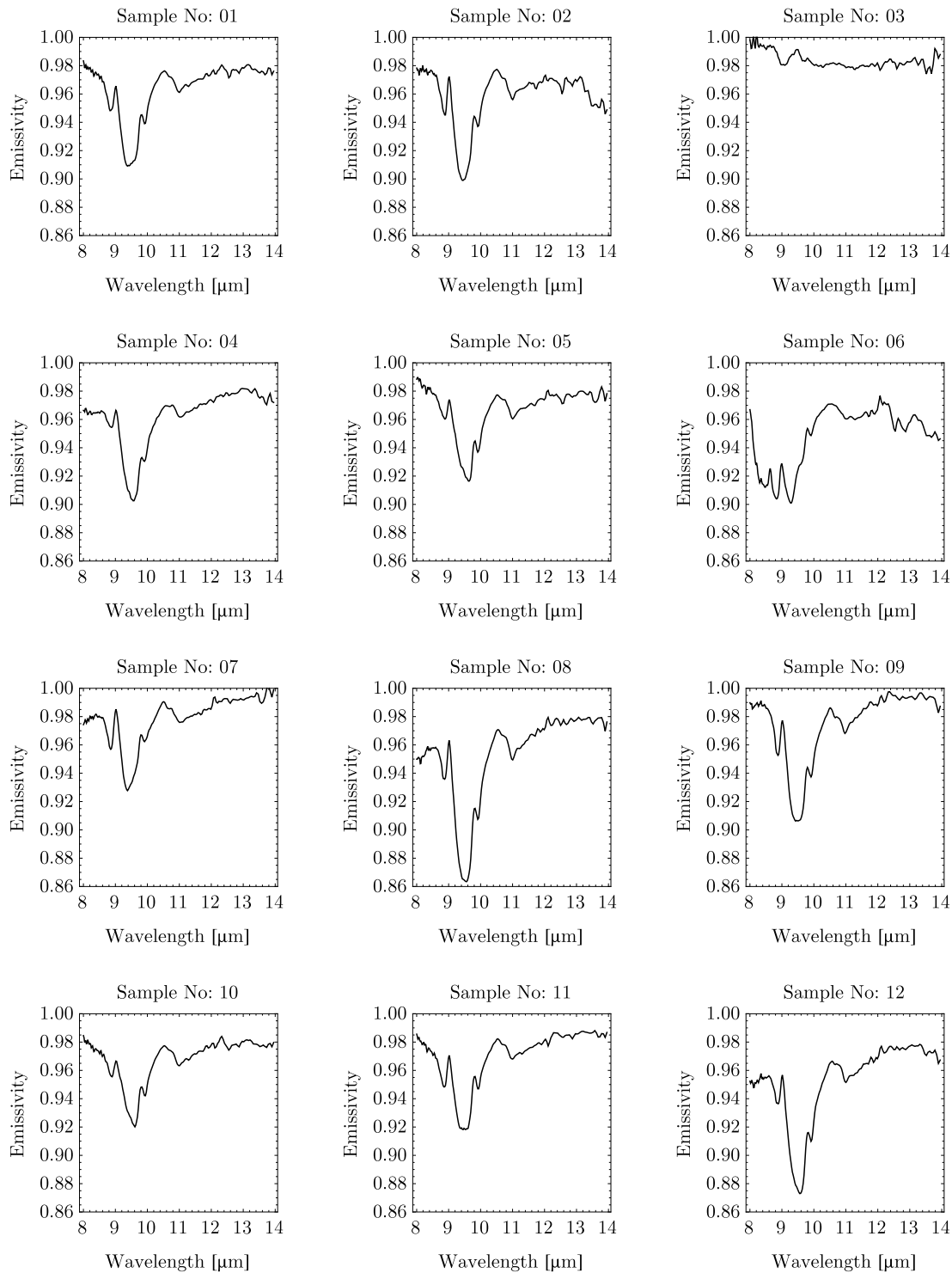
1. toxicity

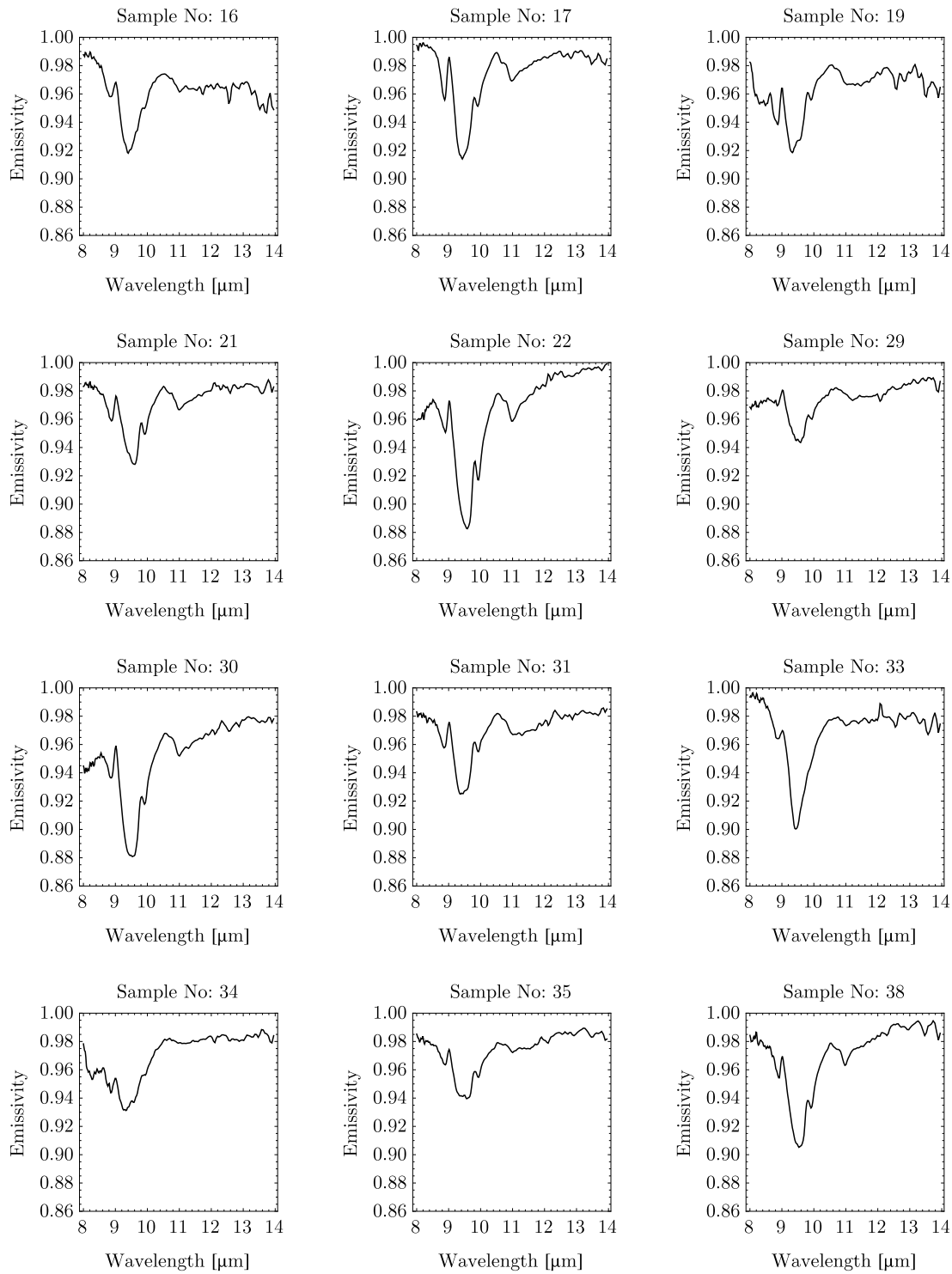
2. pH in H₂O
3. pH in KCl
4. conductivity
5. water soluble Na
6. water soluble K
7. Al in KCl
8. Fe in KCl
9. loss on ignition
10. polyphenol content

A third section contains reference to [15], which discusses toxicity measurement and chemical analysis. Finally, the fourth header section contains the names of two columns, in which the following spectral emissivity data are aligned. Metadata in each header line contains an attribute name followed by a colon (ASCII Character 3A) and tab (ASCII Character 09) and then the corresponding value.

B.2. Spectral Emissivity

After the header part, the file continues on lines 27 – 213 with spectral emissivity data aligned in two columns. As header file indicates, the first column contains wavelength in micrometers and the second column contains corresponding emissivity value. Values in each row are separated by tab. The emissivity of each sample is provided in wavelengths interval from 8 μm to 14 μm . Sampling in this interval is non-linear.

**Figure B.1:** TODO.

**Figure B.2:** TODO.

Bibliography

Author's publications

Scientifically less trustable references

Other references

- [1] B. Eng, personal communication, 2015.
- [2] BALDRIDGE, A.M., HOOK, S.J., GROVE, C.I. and RIVERA, G. The ASTER spectral library version 2.0. *Remote Sensing of Environment*. 2009, **113**(4), 711-715. DOI: 10.1016/j.rse.2008.11.007.
- [3] BARDUCCI, A. and PIPPI, I. Temperature and emissivity retrieval from remotely sensed images using the "Grey body emissivity" method. *IEEE Transactions on Geoscience and Remote Sensing*. 1996, **34**(3), 681-695. DOI: 10.1109/36.499748.
- [4] BERK, A., ANDERSON, G.P., ACHARYA, P.K., BERNSTEIN, L.S., MURATOV, L., LEE, J., FOX, M., ADLER-GOLDEN, S.M., CHETWYND, J.H., HOKE, JR. M.L., LOCKWOOD, R.B., GARDNER, J.A., COOLEY, T.W., BOREL, C.C., LEWIS, P.E. and SHETTLE, E.P. MODTRAN5: 2006 update. In: *Algorithms and Technologies for Multispectral, Hyperspectral, and Ultraspectral Imagery XII*. Orlando (Kissimmee), FL, 2006, F2331–F2331. DOI: 10.1117/12.665077.
- [5] BORBAS, E., SEEMANN, S.W., KERN, A., MOY, L., LI, J., GUMLEY, L. and MENZEL, W.P. *MODIS Atmospheric Profile Retrieval - ATBD* [online]. 2011. [cit. 2016-08-10]. Available at: http://modis-atmos.gsfc.nasa.gov/_docs/MOD07_atbd_v7_April2011.pdf
- [6] BOREL, C. Surface emissivity and temperature retrieval for a hyperspectral sensor. In: *IGARSS '98. Sensing and Managing the Environment. 1998 IEEE International Geoscience and Remote Sensing Symposium Proceedings. (Cat. No.98CH36174)*. Seattle, WA: IEEE, 1998, 546-549. DOI: 10.1109/IGARSS.1998.702966.
- [7] BOREL, C. Error analysis for a temperature and emissivity retrieval algorithm for hyperspectral imaging data. *International Journal of Remote Sensing* [online]. 2008, **29**(17-18), 5029-5045. DOI: 10.1080/01431160802036540.
- [8] BRADSHAW, A.D. and HÜTTL, R.F. Future minesite restoration involves a broader approach. *Ecological Engineering*. 2001, **17**(2-3), 87-90. DOI: 10.1016/S0925-8574(00)00149-X. ISSN 09258574.
- [9] CHEVALLIER, F., CHÉRUY, F., SCOTT, N.A. and CHÉDIN, A. A neural network approach for a fast and accurate computation of a longwave radiative budget. *Journal of Applied Meteorology*. 1998, **37**(11), 1385-1397. DOI: 10.1175/1520-0450(1998)037:1385:ANNAFA;2.0.CO;2.

- [10] CHÉDIN, A., SCOTT, N.A., WAHICHE, C. and MOULINIER, P. The improved initialization inversion method: a high resolution physical method for temperature retrievals from satellites of the TIROS-N series. *Journal of Climate and Applied Meteorology*. 1985, **24**(2), 128-143. DOI: 10.1175/1520-0450(1985)024:0128:TIIIMA;2.0.CO;2
- [11] CHRISTENSEN, P.R., BANDFIELD, J.L., HAMILTON, V.E., HOWARD, D.A., LANE, M.D., PIATEK, J.L., RUFF, S.W. and STEFANOV, W.L. A thermal emission spectral library of rock-forming minerals. *Journal of Geophysical Research: Planets*. 2000, **105**(E4), 9735-9739. DOI: 10.1029/1998JE000624.
- [12] CLARK, R.N., SWAYZE, G.A., WISE, R., LIVO, E., HOEFEN, T., KOKALY, R., SUTLEY, S.J. *USGS digital spectral library splib06a* [online]. U.S. Geological Survey, Digital Data Series 231, 2007. [cit. 2016-07-12]. Available at: <http://speclab.cr.usgs.gov/spectral.lib06>
- [13] COLL, C., CASELLES, V., VALOR, E., NICLÒS, R., SÁNCHEZ, J.M., GALVE, J.M. and MIRA, M. Temperature and emissivity separation from ASTER data for low spectral contrast surfaces. *Remote Sensing of Environment*. 2007, **110**(2), 162-175. DOI: 10.1016/j.rse.2007.02.008.
- [14] FERNÁNDEZ-RENAU, A., MEYNART, R., NEECK, S.P., GÓMEZ, J.A., DE MIGUEL, E. and SHIMODA, H. The INTA AHS system. In: *SPIE Proceedings*. Bruges: SPIE, 2005, 471-478. DOI: 10.1117/12.629440.
- [15] FROUZ, J., KRIŠTŮFEK, V., BASTL, J., KALČÍK, J. and VAŇKOVÁ, H. Determination of Toxicity of Spoil Substrates After Brown Coal Mining Using a Laboratory Reproduction Test with Enchytraeus crypticus (Oligochaeta). *Water, Air, & Soil Pollution*. 2005, **162**(1-4), 37-47. DOI: 10.1007/s11270-005-5991-y.
- [16] FROUZ, J., LIVEČKOVÁ, M., ALBRECHTOVÁ, J., CHROŇÁKOVÁ, A., CAJTHAML, T., PIŽL, V., HÁNĚL, L., STARÝ, J., BALDRIAN, P., LHOTÁKOVÁ, Z., ŠIMÁČKOVÁ, H. and CEPÁKOVÁ, Š. Is the effect of trees on soil properties mediated by soil fauna? A case study from post-mining sites. *Forest Ecology and Management*. 2013, **309**, 87-95. DOI: 10.1016/j.foreco.2013.02.013.
- [17] GARCIA-SANTOS, V., VALOR, E., CASELLES, V., MIRA, M., GALVE, J.M. a COLL, C. Evaluation of Different Methods to Retrieve the Hemispherical Down-welling Irradiance in the Thermal Infrared Region for Field Measurements. *IEEE Transactions on Geoscience and Remote Sensing*. 2013, **51**(4), 2155-2165. DOI: 10.1109/TGRS.2012.2209891.
- [18] GILLESPIE, A.R., *Lithologic mapping of silicate rocks using TIMS* [online]. Jet Propulsion Lab., California Inst. of Tech., Pasadena, CA, United States, 1986. [cit. 2016-08-10]. Available at: <http://ntrs.nasa.gov/search.jsp?R=19870007685>
- [19] GILLESPIE, A.R., ABBOTT, E.A., GILSON, L., HULLEY, G., JIMÉNEZ-MUÑOZ, J.C. and SOBRINO, J.A. Residual errors in ASTER temperature and emissivity standard products AST08 and AST05. *Remote Sensing of Environment*. 2011, **115**(12), 3681-3694. DOI: 10.1016/j.rse.2011.09.007.

- [20] GILLESPIE, A.R., ROKUGAWA, S., HOOK, S., MATSUNAGA, T. and KAHLE, A.B. *Temperature/Emissivity Separation Algorithm Theoretical Basis Document, Version 2.4* [online]. Pasadena: Jet Propulsion Laboratory, 1999. [cit. 2016-01-19]. Available at: <http://eospso.nasa.gov/sites/default/files/atbd/atbd-ast-05-08.pdf>
- [21] GILLESPIE, A.R., ROKUGAWA, S., MATSUNAGA, T., COTHERN, J.S., HOOK, S. and KAHLE, A.B. A temperature and emissivity separation algorithm for Advanced Spaceborne Thermal Emission and Reflection Radiometer (ASTER) images. *IEEE Transactions on Geoscience and Remote Sensing*. 1998, **36**(4), 1113-1126. DOI: 10.1109/36.700995.
- [22] GU, D., GILLESPIE, A.R., KAHLE, A.B. and PALLUCONI, F.D. Autonomous atmospheric compensation (AAC) of high resolution hyperspectral thermal infrared remote-sensing imagery. *IEEE Transactions on Geoscience and Remote Sensing*. 2000, **38**(6), 2557-2570. DOI: 10.1109/36.885203.
- [23] GUSTAFSON, W.T., GILLESPIE, A.R. and YAMADA, G.J. Revisions to the ASTER temperature/emissivity separation algorithm. In: *Second Recent Advances in Quantitative Remote Sensing*. Valencia, 2006, 770-775.
- [24] HANUŠ, J., FABIÁNEK, T., KAPLAN, V. and HOMOLOVÁ, L. Flying laboratory of imaging systems (FLIS) at CzechGlobe. In: *SGEM2014 Conference Proceedings*. 2014, 177-182. DOI: 10.5593/SGEM2014/B23/S10.022. ISBN 978-619-7105-12-4. ISSN 1314-2704.
- [25] HAMOUZ, K., LACHMAN, J., PIVEC, V. and ORSÁK, M. The effect of the conditions of cultivation on the content of polyphenol compounds in the potato varieties Agria and Karin. *Rostlinná Výroba*. 1997, **43**, 541-546.
- [26] HOOK, S.J. and KAHLE, A.B. The micro fourier transform interferometer (uFTIR) — A new field spectrometer for acquisition of infrared data of natural surfaces. *Remote Sensing of Environment*. 1996, **56**(3), 172-181. DOI: 10.1016/0034-4257(95)00231-6.
- [27] HORTON, K.A., JOHNSON, J.R. and LUCEY, P.G. Infrared Measurements of Pristine and Disturbed Soils 2. Environmental Effects and Field Data Reduction. *Remote Sensing of Environment*. 1998, **64**(1), 47-52. DOI: 10.1016/S0034-4257(97)00167-3.
- [28] HOWELL, J.R. *Thermal radiation heat transfer*. 5th ed. Boca Raton: CRC Press, c2011. 957. ISBN 978-1-4398-0533-6.
- [29] HULLEY, G. and HOOK, S.J. Generating Consistent Land Surface Temperature and Emissivity Products Between ASTER and MODIS Data for Earth Science Research. *IEEE Transactions on Geoscience and Remote Sensing*. 2011, **49**(4), 1304-1315. DOI: 10.1109/TGRS.2010.2063034.
- [30] HULLEY, G. and HOOK, S.J. *HyspIRI Level-2 Thermal Infrared (TIR) Land Surface Temperature and Emissivity Algorithm Theoretical Basis Document* [online]. Pasadena, California: Jet Propulsion Laboratory, California Institute of Technology, 2011. [cit. 2016-01-19]. Available at:

https://hyspiri.jpl.nasa.gov/downloads/Algorithm_Theoretical_Basis/HyspIRI_L2_Surface_Temperature_Emissivity_JPL_Pub_11-5_10102011.pdf

- [31] ITRES. SparCal [software]. [access 1.3.2016]. Available at: <http://www.itres.com/supporting-products/>
- [32] ITRES. RCX [software]. [access 1.3.2016]. Available at: <http://www.itres.com/supporting-products/>
- [33] ITRES. GCSS [software]. [access 1.3.2016]. Available at: <http://www.itres.com/supporting-products/>
- [34] JIMÉNEZ-MUÑOZ, J.C., CRISTOBAL, J., SOBRINO, J.A., SORIA, G., NINYEROLA, M. and PONS, X. Revision of the Single-Channel Algorithm for Land Surface Temperature Retrieval From Landsat Thermal-Infrared Data. *IEEE Transactions on Geoscience and Remote Sensing*. 2009, **47**(1), 339-349. DOI: 10.1109/TGRS.2008.2007125.
- [35] JIMÉNEZ-MUÑOZ, J.C., SOBRINO, J.A. and GILLESPIE, A.R. Surface Emissivity Retrieval From Airborne Hyperspectral Scanner Data: Insights on Atmospheric Correction and Noise Removal. *IEEE Geoscience and Remote Sensing Letters*. 2012, **9**(2), 180-184. DOI: 10.1109/LGRS.2011.2163699.
- [36] JIMÉNEZ-MUÑOZ, J.C., SOBRINO, J.A., MATTAR, C., HULLEY, G. and GOTTSCHE, F.-M. Temperature and Emissivity Separation From MSG/SEVIRI Data. *IEEE Transactions on Geoscience and Remote Sensing*. 2014, **52**(9), 5937-5951. DOI: 10.1109/TGRS.2013.2293791.
- [37] JONES, J.B. *Agronomic handbook: management of crops, soils, and their fertility*. Boca Raton, Fla.: CRC Press, c2003. ISBN 0849308976.
- [38] KIRCHHOFF, G. Ueber das Verhältniss zwischen dem Emissionsvermögen und dem Absorptionsvermögen der Körper für Wärme und Licht. *Annalen der Physik und Chemie*. 1860, **185**(2), 275-301. DOI: 10.1002/andp.18601850205.
- [39] KOTTHAUS, S., SMITH, T.E.L., WOOSTER, M.J. and GRIMMOND, C.S.B. Derivation of an urban materials spectral library through emittance and reflectance spectroscopy. *ISPRS Journal of Photogrammetry and Remote Sensing*. 2014, **94**, 194-212. DOI: 10.1016/j.isprsjprs.2014.05.005.
- [40] LI, Z., TANG, B., WU, H., REN, H., YAN, G., WAN, Z., TRIGO, I.F. and SOBRINO, J.A. Satellite-derived land surface temperature: Current status and perspectives. *Remote Sensing of Environment* [online]. 2013, **131**, 14-37. DOI: 10.1016/j.rse.2012.12.008.
- [41] MATSUNAGA, T. A Temperature-Emissivity Separation Method Using an Empirical Relationship between the Mean, the Maximum, and the Minimum of the Thermal Infrared Emissivity Spectrum. *Journal of the Remote Sensing Society of Japan*. 1994, **14**(3), 230–241. DOI: 10.11440/rssj1981.14.230

- [42] MUSHKIN, A., BALICK, L.K., and GILLESPIE, A.R. Temperature/emissivity separation of MTI data using the Terra/ASTER TES algorithm. In: *Algorithms and Technologies for Multispectral, Hyperspectral, and Ultraspectral Imagery VIII*. Orlando, FL: SPIE, 2002, 328-337. DOI: 10.1117/12.478764.
- [43] NOTESCO, G., KOPAČKOVÁ, V., ROJÍK, P., SCHWARTZ, G., LIVNE, I. and DOR, E. Mineral Classification of Land Surface Using Multispectral LWIR and Hyperspectral SWIR Remote-Sensing Data. A Case Study over the Sokolov Lignite Open-Pit Mines, the Czech Republic. *Remote Sensing*. 2014, **6**(8), 7005-7025. DOI: 10.3390/rs6087005.
- [44] PASCUCCI, S., CASA, R., BELVISO, C., PALOMBO, A., PIGNATTI, S. and CASTALDI, F. Estimation of soil organic carbon from airborne hyperspectral thermal infrared data: a case study. *European Journal of Soil Science*. 2014, **65**(6), 865-875. DOI: 10.1111/ejss.12203.
- [45] PIPIA, L., PEREZ, F., TARDA, A., MARTINEZ, L. and ARBIOL, R. Simultaneous usage of optic and thermal hyperspectral sensors for crop water stress characterization. In: *IEEE International Geoscience and Remote Sensing Symposium*. Munich: IEEE, 2012, 6661-6664. DOI: 10.1109/IGARSS.2012.6352071.
- [46] PLANCK, M. Zur Theorie des Gesetzes der Energieverteilung im Normalspektrum. *Verhandlungen der Deutschen Physikalischen Gesellschaft*. 1900, **2**(17), p. 237-245.
- [47] RIBEIRO DA LUZ, B. and CROWLEY, J.K. Identification of plant species by using high spatial and spectral resolution thermal infrared (8.0–13.5 μm) imagery. *Remote Sensing of Environment*. 2010, **114**(2), 404-413. DOI: 10.1016/j.rse.2009.09.019.
- [48] RICHTER, R. a SCHLÄPFER, D. Geo-atmospheric processing of airborne imaging spectrometry data. Part 2: Atmospheric/topographic correction. *International Journal of Remote Sensing*. 2002, **23**(13), 2631-2649. DOI: 10.1080/01431160110115834.
- [49] SABOL, Jr., D.E., GILLESPIE, A.R., ABBOTT, E. and YAMADA, G. Field validation of the ASTER Temperature–Emissivity Separation algorithm. *Remote Sensing of Environment*. 2009, **113**(11), 2328-2344. DOI: 10.1016/j.rse.2009.06.008.
- [50] SALISBURY, J.W., WALTER, L.S., VERGO, N., D'ARIA, D.M. *Infrared (2.1-25 um) spectra of minerals*. Baltimore: John Hopkins University Press, 1991. ISBN 0801844398.
- [51] SHUKLA, M. K. a R. LAL. Temporal Changes in Soil Organic Carbon Concentration and Stocks in Reclaimed Minesoils of Southeastern Ohio. *Soil Science*. 2005, **170**(12), 1013-1021. DOI: 10.1097/01.ss.0000187354.62481.91.
- [52] SNYDER, W. C., WAN, Z., ZHANG, Y. and FENG, Y.-Z. Classification-based emissivity for land surface temperature measurement from space. *International Journal of Remote Sensing*. 1998, **19**(14), 2753-2774. DOI: 10.1080/014311698214497.
- [53] SOBRINO, J.A., FRANCH, B., MATTAR, C., JIMÉNEZ-MUÑOZ, J.C. and CORBARI, C. A method to estimate soil moisture from Airborne Hyperspectral Scanner

- (AHS) and ASTER data: Application to SEN2FLEX and SEN3EXP campaigns. *Remote Sensing of Environment*. 2012, **117**, 415–428. DOI: 10.1016/j.rse.2011.10.018
- [54] SOBRINO, J.A., JIMÉNEZ-MUÑOZ, J.C., BALICK, L., GILLESPIE, A.R., SABOL, D., and GUSTAFSON, W. Accuracy of ASTER Level-2 thermal-infrared Standard Products of an agricultural area in Spain. *Remote Sensing of Environment*. 2007, **106**(2), 146-153. DOI: 10.1016/j.rse.2006.08.010. ISSN 00344257.
 - [55] SOBRINO, J.A., JIMÉNEZ-MUÑOZ, J.C., LABED-NACHBRAND, J. and NERRY, F. Surface emissivity retrieval from Digital Airborne Imaging Spectrometer data. *Journal of Geophysical Research: Atmospheres*. 2002, **107**(D23). DOI: 10.1029/2002JD002197.
 - [56] SOBRINO, J.A., JIMÉNEZ-MUÑOZ, J.C., ZARCO-TEJADA, P.J., SEPULCRE-CANTÓ, G. and DE MIGUEL, E. Land surface temperature derived from airborne hyperspectral scanner thermal infrared data. *Remote Sensing of Environment*. 2006, **102**(1-2), 99-115. DOI: 10.1016/j.rse.2006.02.001.
 - [57] SOBRINO, J.A., MATTAR, C., PARDO, P., JIMÉNEZ-MUÑOZ, J.C., HOOK, S.J., BALDRIDGE, A. and IBAÑEZ, R. Soil emissivity and reflectance spectra measurements. *Applied Optics*. 2009, **48**(19), 3664-3670. DOI: 10.1364/AO.48.003664.
 - [58] SOBRINO, J.A., OLTRA-CARRIÓN, R., JIMÉNEZ-MUÑOZ, J.C., JULIEN, Y., SORIA, G., FRANCH, B. and MATTAR, C. Emissivity mapping over urban areas using a classification-based approach: Application to the Dual-use European Security IR Experiment (DESIREX). *International Journal of Applied Earth Observation and Geoinformation*. 2012, **18**, 141–147. DOI: 10.1016/j.jag.2012.01.022.
 - [59] SOBRINO, J.A. and RAISOUNI, N. Toward remote sensing methods for land cover dynamic monitoring: Application to Morocco. *International Journal of Remote Sensing*. 2000, **21**(2), 353-366. DOI: 10.1080/014311600210876.
 - [60] SORIA, G. and J.A. SOBRINO. ENVISAT/AATSR derived land surface temperature over a heterogeneous region. *Remote Sensing of Environment*. 2007, **111**(4), 409-422. DOI: 10.1016/j.rse.2007.03.017.
 - [61] TONOOKA, H. Accurate atmospheric correction of ASTER thermal infrared imagery using the WVS method. *IEEE Transactions on Geoscience and Remote Sensing*. 2005, **43**(12), 2778-2792. DOI: 10.1109/TGRS.2005.857886.
 - [62] TONOOKA, H. and PALLUCONI, D. Verification of the ASTER/TIR atmospheric correction algorithm based on water surface emissivity retrieved. In: *Proceedings of the Society of Photo-optical Instrumentation Engineers*. San Diego, CA: SPIE, 2001, 51-58. DOI: 10.1117/12.455143.
 - [63] TONOOKA, H. and PALLUCONI, D. Validation of ASTER/TIR standard atmospheric correction using water surfaces. *IEEE Transactions on Geoscience and Remote Sensing*. 2005, **43**(12), 2769-2777. DOI: 10.1109/TGRS.2005.857883.

- [64] TONOOKA, H., PALLUCONI, D., HOOK, S.J. and MATSUNAGA, T. Vicarious calibration of ASTER thermal infrared bands. *IEEE Transactions on Geoscience and Remote Sensing*. 2005, **43**(12), 2733-2746. DOI: 10.1109/TGRS.2005.857885.
- [65] USSIRI, D.A.N., LAL, R. and JACINTHE, P.-A. Post-reclamation Land Use Effects on Properties and Carbon Sequestration in Minesoils of Southeastern Ohio. *Soil Science*. 2006, **171**(3), 261-271. DOI: 10.1097/01.ss.0000199702.68654.1e.
- [66] Edited by VAN DER MEER, F.D. and DE JONG, S.M. *Imaging Spectrometry: Basic Principles and Prospective Applications*. Dordrecht: Kluwer Academic Publishers, 2001. ISBN 978-0-306-47578-8.
- [67] VINDUŠKOVÁ, O. a FROUZ, J. Soil carbon accumulation after open-cast coal and oil shale mining in Northern Hemisphere: a quantitative review. *Environmental Earth Sciences*. 2013, **69**(5), 1685-1698. DOI: 10.1007/s12665-012-2004-5.
- [68] WAN, Z. New refinements and validation of the MODIS Land-Surface Temperature/Emissivity products. *Remote Sensing of Environment*. 2008, **112**(1), 59-74. DOI: 10.1016/j.rse.2006.06.026.
- [69] WANG, N., WU, H., NERRY, H., LI, C. and LI, Z. Temperature and Emissivity Retrievals From Hyperspectral Thermal Infrared Data Using Linear Spectral Emissivity Constraint. *IEEE Transactions on Geoscience and Remote Sensing*. 2011, **49**(4), 1291-1303. DOI: 10.1109/TGRS.2010.2062527.
- [70] WANG, H., XIAO, Q., LI, H. and ZHONG, B. Temperature and emissivity separation algorithm for TASI airborne thermal hyperspectral data. In: *2011 International Conference on Electronics, Communications and Control (ICECC)*. Ningbo: IEEE, 2011, 1075-1078. DOI: 10.1109/icecc.2011.6066288.
- [71] YOUNG, S.J. An in-scene method for atmospheric compensation of thermal hyperspectral data. *Journal of Geophysical Research*. 2002, **107**(D24). DOI: 10.1029/2001jd001266.
- [72] Edited by ZEMEK, F.. *Airborne remote sensing: theory and practice in assessment of terrestrial ecosystems*. Brno: Global Change Research Institute CAS, 2014. 159. ISBN 978-80-87902-05-9.
- [73] VAN DER MEER, F.D., VAN DER WERFF, H.M.A., VAN RUITENBEEK, F.J.A., et al. Multi- and hyperspectral geologic remote sensing: A review. *International Journal of Applied Earth Observation and Geoinformation*. 2012, **14**(1), 112-128. DOI: 10.1016/j.jag.2011.08.002.
- [74] PIERI, D. and ABRAMS, M. ASTER watches the world's volcanoes: a new paradigm for volcanological observations from orbit. *Journal of Volcanology and Geothermal Research*. 2004, **135**(1-2), 13-28. DOI: 10.1016/j.jvoleores.2003.12.018
- [75] FOSTER, L.A., BROCK, B.W., CUTLER, M.E.J. and DIOTRI, F. A physically based method for estimating supraglacial debris thickness from thermal band remote-sensing data. *Journal of Glaciology*. 2012, **58**(210), 677-691. DOI: 10.3189/2012JoG11J194.

- [76] SCHEIDT, S., RAMSEY, M. and LANCASTER, N. Determining soil moisture and sediment availability at White Sands Dune Field, New Mexico, from apparent thermal inertia data. *Journal of Geophysical Research: Earth Surface*. 2010, **115**(F2). DOI: 10.1029/2009JF001378.
- [77] WENG, Q., RAJASEKAR, U. and HU, X. Modeling Urban Heat Islands and Their Relationship With Impervious Surface and Vegetation Abundance by Using ASTER Images. *IEEE Transactions on Geoscience and Remote Sensing*. 2011, **49**(10), 4080-4089. DOI: 10.1109/TGRS.2011.
- [78] FRENCH, A., SCHMUGGE, T., RITCHIE, J., HSU, A., JACOB, F. and OGAWA, K. Detecting land cover change at the Jornada Experimental Range, New Mexico with ASTER emissivities. *Remote Sensing of Environment*. 2008, **112**(4), 1730-1748. DOI: 10.1016/j.rse.2007.08.020.